Ocean Modelling xxx (2015) xxx–xxx

Contents lists available at ScienceDirect

Ocean Modelling

journal homepage: www.elsevier.com/locate/ocemod

Impacts of regional mixing on the temperature structure of the equatorial Pacific Ocean. Part 1: Vertically uniform vertical diffusion ☆

Ryo Furue [a,e,*], Yanli Jia [a], Julian P. McCreary [a], Niklas Schneider [a], Kelvin J. Richards [a], Peter Müller [b], Bruce D. Cornuelle [c], Nidia Martínez Avellaneda [c], Detlef Stammer [d], Chuanyu Liu [d], Armin Köhl [d]

[a] International Pacific Research Center, University of Hawaii, Honolulu, HI, USA
[b] Department of Oceanography, University of Hawaii, Honolulu, HI, USA
[c] Scripps Institution of Oceanography, La Jolla, CA, USA
[d] Institute of Oceanography, University of Hamburg, Hamburg, Germany
[e] Application Laboratory, JAMSTEC, Yokohama, Japan

ARTICLE INFO

Article history:
Received 20 November 2013
Received in revised form 30 September 2014
Accepted 5 October 2014
Available online xxxx

Keywords:
Diffusion
Rossby waves
Kelvin waves
Advection
Pycnocline
Ocean general circulation models

ABSTRACT

We investigate the sensitivity of numerical-model solutions to regional changes in vertical diffusion. Specifically, we vary the background diffusion coefficient, κ_b, within spatially distinct subregions of the tropical Pacific, assess the impacts of those changes, and diagnose the processes that account for them.

Solutions respond to a diffusion anomaly, $\delta\kappa_b$, in three ways. Initially, there is a fast response (several months), due to the interaction of rapidly-propagating, barotropic and gravity waves with eddies and other mesoscale features. It is followed by a local response (roughly one year), the initial growth and spatial pattern of which can be explained by one-dimensional (vertical) diffusion. At this stage, temperature and salinity anomalies are generated that are either associated with a change in density ("dynamical" anomalies) or without one ("spiciness" anomalies). In a final adjustment stage, the dynamical and spiciness anomalies spread to remote regions by radiation of Rossby and Kelvin waves and by advection, respectively.

In near-equilibrium solutions, dynamical anomalies are generally much larger in the latitude band of the forcing, but the impact of off-equatorial forcing by $\delta\kappa_b$ on the equatorial temperature structure is still significant. Spiciness anomalies spread equatorward within the pycnocline, where they are carried to the equator as part of the subsurface branch of the Pacific Subtropical Cells, and spiciness also extends to the equator via western-boundary currents. Forcing near and at the equator generates strong dynamical anomalies, and sometimes additional spiciness anomalies, at pycnocline depths. The total response of the equatorial temperature structure to $\delta\kappa_b$ in various regions depends on the strength and spatial pattern of the generation of each signal within the forcing region as well as on the processes of its spreading to the equator.

© 2014 The Authors. Published by Elsevier Ltd. This is an open access article under the CC BY-NC-SA license (http://creativecommons.org/licenses/by-nc-sa/3.0/).

1. Introduction

Ocean general circulation models (OGCMs) often misrepresent basic features of the density field in the tropical Pacific Ocean, including (i) the location and intensity of the cold tongue in the eastern, equatorial ocean and (ii) the sharpness of the tropical thermocline and near-equatorial fronts. These deficiencies are consequential in that they may lead to errors in simulations of climate variability by coupled general circulation models, for example, contributing to inaccurate representations of near-equatorial currents and the strength and time scale of El Niño–Southern Oscillation (ENSO). A possible cause for these stratification errors is inaccurate parameterizations of mixing processes. The parameterization of subsurface vertical (diapycnal) diffusion is particularly important because it can modify density and pressure, and hence is dynamically active. Furthermore, resolving the small-scale processes responsible for vertical mixing (e.g., Kelvin-Helmholtz instability, internal wave breaking) in OGCMs is impossible in the foreseeable future, and so improving vertical-mixing parameterizations remains a first-order problem.

Parameterizations of subsurface vertical diffusion are commonly represented by a background diffusivity with a coefficient, κ_b, that is constant everywhere or a prescribed function of depth.

☆ The paper is SOEST Contribution 2909 and IPRC Contribution 1081.

* Corresponding author at: JAMSTEC, 3173-25 Showa-machi, Kanazawa-ku, Yokohama 236-0001, Japan. Tel.: +81 45 778 5497.
E-mail address: furue@hawaii.edu (R. Furue).

http://dx.doi.org/10.1016/j.ocemod.2014.10.002
1463-5003/© 2014 The Authors. Published by Elsevier Ltd.
This is an open access article under the CC BY-NC-SA license (http://creativecommons.org/licenses/by-nc-sa/3.0/).

Please cite this article in press as: Furue, R., et al. Impacts of regional mixing on the temperature structure of the equatorial Pacific Ocean. Part 1: Vertically uniform vertical diffusion. Ocean Modell. (2015), http://dx.doi.org/10.1016/j.ocemod.2014.10.002

Recently, parameterizations have been tested in which κ_b is allowed to vary spatially, for example, depending on external variables such as mean tidal amplitude, bottom roughness, features of the ocean circulation, or geographical location (e.g., Hasumi and Suginohara, 1999; Jayne and St. Laurent, 2001; Friedrich et al., 2011). The majority of these studies are concerned about effects of vertical mixing in the deep ocean.

Several studies have begun to explore how regional changes in κ_b impact the upper, tropical ocean. It has been recognized that, below the mixed layer and within the region in which κ_b is changed, the response of the stratification (temperature or density) is qualitatively consistent with changes generated locally by the anomalous, vertical diffusive flux (e.g., Richards et al., 2009; Jochum, 2009). Anomalies generated by such local processes are then propagated to other regions by advection, diffusion, or wave radiation. In particular, it has been suggested that off-equatorial effects of diffusion are propagated to the equator by the Pacific Subtropical Cells (STCs; McCreary and Lu, 1994) through advection in the main pycnocline (e.g., Jochum, 2009; Tatebe and Hasumi, 2010; Manucharyan et al., 2011). The equatorial stratification anomalies due to local and remote κ_b changes affect the climate state and variability such as ENSO in atmosphere-ocean coupled models (Meehl et al., 2001; Richards et al., 2009; Jochum, 2009; Manucharyan et al., 2011; Sasaki et al., 2013; Kim et al., 2014).

In this paper, we continue the effort to understand impacts of spatially-varying vertical diffusion in the tropical Pacific. Our goal is to understand the basic processes by which the ocean responds both locally and remotely to changes in κ_b in different regions. For one thing, this knowledge allows the identification of regions where vertical mixing has the greatest impact on important aspects of the ocean state, such as tropical sea surface temperature (SST). For another, it will help in the development of new κ_b parameterizations, by allowing researchers to understand better how the parameterization will impact the ocean state.

We consider κ_b anomalies that are depth independent, the simplest choice when not dealing with particular mixing processes. (We will consider the impact of depth-dependent κ_b anomalies in a companion study; see the discussion at the end of Section 4.) Our approach is to obtain a set of OGCM solutions in which κ_b is increased from a standard value κ_0 to $\kappa_0 + \delta\kappa_b(x,y)$ in spatially distinct subregions of the tropical Pacific, to assess the impact of those changes, and to diagnose the processes that cause them. A particular focus is on how $\delta\kappa_b$ affects the equatorial temperature structure, because the mean climate and its variability are known to be sensitive to that structure. An important aspect of our analysis is that we split temperature anomalies into parts that are either associated with a density change (dynamical anomaly) or without one (spiciness anomaly). As we shall see, these anomalies differ locally from region to region, and they propagate about the basin in very different ways, namely, by radiation of Rossby and Kelvin waves and by advection, respectively.

The paper is organized as follows. Section 2 reports our overall experimental design and describes the various measures that we use to quantify differences between model solutions. Section 3 describes our control run, discusses the processes that adjust solutions to equilibrium in response to forcing by $\delta\kappa_b$, describes the stratification anomalies that develop in several of the regional solutions, and reports the contribution of individual solutions to equatorial SST. Section 4 provides a summary and discussion of results. Appendix A gives precise definitions of the measures of differences, describes how we calculate them, and discusses their properties. Appendix B discusses the properties of regional solutions not reported in Section 3.

2. Experimental design

This section reports our overall approach. We first describe our ocean model and then the suite of solutions that we obtain. We conclude by defining the various measures of solution differences that we use in Section 3.

2.1. Ocean model

We use the Massachusetts Institute of Technology general circulation model (MITgcm; Marshall et al., 1997), which solves the incompressible Navier-Stokes equations on a sphere in a hydrostatic mode with an implicit free surface. Our model set-up is based on Hoteit et al. (2008) and Hoteit et al. (2010) with several modifications. The model domain covers the tropical and subtropical Pacific from 26°S–30°N and 104°E–70°W (see Fig.1), with a constant resolution of $1/3^\circ$ in both the zonal and meridional directions. The model ocean depth and domain boundaries are defined by the ETOPO2 database (http://www.ngdc.noaa.gov/mgg/global/etopo2.html), the latter defined by the 10-m contour with additional manual editing to remove singular water points. Topography in the Indonesian Seas is also manually edited to allow for reasonable mean transports through narrow channels (e.g., McCreary et al., 2007). The model's vertical resolution ranges from 5 m near the surface to 510 m near the bottom with a total of 51 layers.

Closed, no-slip conditions are specified at land boundaries, and a quadratic form of bottom friction with a drag coefficient of 0.002 is applied. The artificial, northern and southern boundaries, as well as a portion of the western boundary located in the Indian Ocean, are open. Near these boundaries, model variables (temperature, salinity, and horizontal velocity) are relaxed to a monthly climatology determined from the German partner of the consortium for Estimating the Circulation and Climate of the Ocean (GECCO) reanalysis (Köhl et al., 2007; Köhl and Stammer, 2008). Specifically, model variables are relaxed to GECCO values at time scales that vary from 1–20 days within 3° of the boundaries.

Subgrid-scale horizontal mixing is parameterized by biharmonic operators with constant coefficients of 4×10^{11} m^4 s^{-1} for viscosity and 2×10^{11} m^4 s^{-1} for tracer diffusion. The K-profile parameterization of Large et al. (1994) is used for vertical mixing, with background coefficients of 10^{-4} m^2 s^{-1} for viscosity and, for our

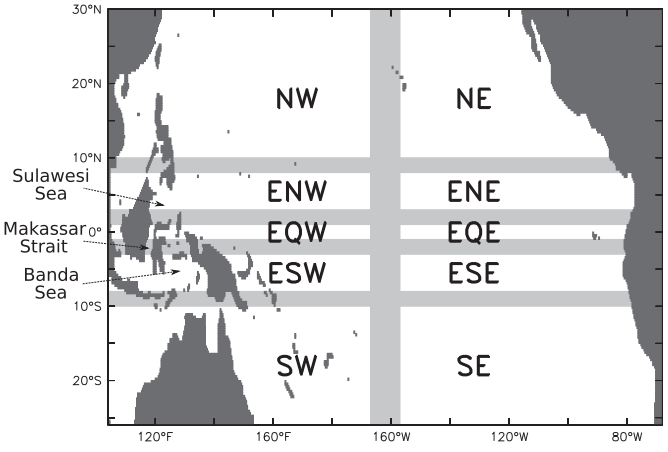

Fig. 1. The model domain showing each geographical region where κ_b is increased from the standard value $\kappa_0 = 0.1 \times 10^{-4}$ m^2 s^{-1} to $\kappa_0 + \Delta\kappa = 0.5 \times 10^{-4}$ m^2 s^{-1}. The gray bands are ramp regions, within which κ_b is ramped sinusoidally from κ_0 to $\kappa_0 + \Delta\kappa$. Precise specifications of these experiments are found in Table 1 and in the text. Two solutions not indicated are Solution CTL (control run) with $\kappa_b = \kappa_0$ everywhere and Solution FB (full basin) in which $\kappa_b = \kappa_0 + \Delta\kappa$ everywhere. Geographical names in the Indonesian Seas are shown for reference in Section 3.3.

Please cite this article in press as: Furue, R., et al. Impacts of regional mixing on the temperature structure of the equatorial Pacific Ocean. Part 1: Vertically uniform vertical diffusion. Ocean Modell. (2015), http://dx.doi.org/10.1016/j.ocemod.2014.10.002

control run, 0.1×10^{-4} m^2 s^{-1} for diffusion (κ_b). Parameter κ_b is then altered in sensitivity experiments (see Section 2.2).

Surface forcing is determined from a monthly climatology of atmospheric variables from the European Centre for Medium Range Weather Forecasts (ECMWF) Interim Reanalysis (ERA-Interim, http://apps.ecmwf.int/datasets/data/interim_full_daily) for the period of 1991–2000. These variables are used to compute surface turbulent and radiative fluxes for the ocean model by the bulk formulae of Large and Pond (1981) and Large and Pond (1982), according to which sea-surface heat flux and evaporation depend on sea-surface temperature.

Our control experiment (CTL) is initialized with the January climatology of the GECCO reanalysis, and integrated for 40 years to reach a quasi-equilibrium state in the upper ocean. Each of the subsequent experiments (CTL and sensitivity experiments) is then initialized with the year-40 state of CTL and integrated forward for an additional 20 years. In all the experiments, the ERA-interim and GECCO climatologies are repeatedly used for all model years. Unless stated otherwise, solutions discussed in the text and shown in figures are taken from the final year of integration. By this time, solutions are approaching equilibrium throughout the basin, particularly so near the equator.

2.2. Solutions

Table 1 lists the experiments we carry out. Experiment CTL is our control run in which κ_b is set everywhere to the default value $\kappa_0 = 0.1 \times 10^{-4}$ m^2 s^{-1}. In experiment FB, κ_b is increased to $\kappa_0 + \Delta\kappa = 0.5 \times 10^{-4}$ m^2 s^{-1} throughout the basin. In the other experiments, κ_b is increased from κ_0 to $\kappa_0 + \Delta\kappa$ within specified subregions. As shown in Fig. 1, the regions are located in the eastern and western ocean, near the equator (EQE and EQW; equatorial regions), to either side of the equator (ENE, ENW, ESE, and ESW; off-equatorial regions), and poleward of 8°S or 8°N (NE, NW, SE, and SW; tropical regions).

Just inside the edges of each subregion, κ_b is ramped from κ_0 to $\kappa_0 + \Delta\kappa$ using cosine tapers of the form

$$r_{\binom{1}{2}}(\eta) = (1 \pm \cos\pi\eta)/2, \quad 0 \leqslant \eta \leqslant 1, \tag{1}$$

where η is a non-dimensional coordinate with a different form for each type of edge. According to (1), r_1 decreases from 1 to 0 with η and vice versa for r_2.

Table 1
List of experiments.

Exp.	Subregion		max κ_b
	Lat. range	Lon. range	(10^{-4} m^2 s^{-1})
CTL	Full basin		0.1
FB	Full basin		0.5
SE	< 8°S	> 157°W	0.5
SW	< 8°S	< 167°W	0.5
NE	> 8°N	> 157°W	0.5
NW	> 8°N	< 167°W	0.5
ESE	10°–1°S	> 157°W	0.5
ESW	10°–1°S	< 167°W	0.5
ENE	1°–10°N	> 157°W	0.5
ENW	1°–10°N	< 167°W	0.5
EQE	3°S–3°N	> 155°W	0.5
EQW	3°S–3°N	< 167°W	0.5

For each experiment, rows provide its label, the edges of the subregions where κ_b is increased, and the maximum diffusivity. Coefficient κ_b either has a constant value throughout the basin (full basin) or its value increases from κ_0 to $\kappa_0 + \Delta\kappa$ in ramps just inside the edges of each subregion (see text and Fig. 1).

Consider such a ramp just inside the eastern edge of a subregion and let x_1 be the point where κ_b starts to decrease. Then, κ_b decreases from $\kappa_0 + \Delta\kappa$ to κ_0 across the ramp as

$$\kappa_b(x) = \kappa_0 + \Delta\kappa\, r_1\left(\frac{x - x_1}{\Delta x}\right), \quad x_1 \leqslant x \leqslant x_1 + \Delta x. \tag{2}$$

Similarly, for the western edge of a subregion κ_b increases from κ_0 to $\kappa_0 + \Delta\kappa$ across the ramp as

$$\kappa_b(x) = \kappa_0 + \Delta\kappa\, r_2\left(\frac{x - x_2}{\Delta x}\right), \quad x_2 \leqslant x \leqslant x_2 + \Delta x, \tag{3}$$

where x_2 is the point where κ_b starts to increase. Ramps inside the northern and southern edges are similar with $\eta = (y - y_j)/\Delta y$. Just inside the corner of a subregion, a two-dimensional ramp is necessary. There,

$$\kappa_b(x,y) = \kappa_0 + \Delta\kappa\, r_i\left(\frac{x - x_i}{\Delta x}\right) r_j\left(\frac{y - y_j}{\Delta y}\right), \quad x_i \leqslant x \leqslant x_i + \Delta x, \quad y_j \leqslant y \leqslant y_j + \Delta y, \tag{4}$$

where $(i,j) = (1,1), (2,1), (2,2), (1,2)$ for northeast, northwest, southwest, and southeast corners.

With the choices $\Delta x = 10°$ and $\Delta y = 2°$, ramps of adjacent subregions overlap by Δx and Δy, as indicated in Table 1 and Fig. 1. Note that, with the above definitions, the sum of the kappa "anomalies" ($\delta\kappa_b \equiv \kappa_b - \kappa_0$) in adjacent regions is κ_b where they overlap (for both edges and corners). It follows that, when the $\delta\kappa_b(x,y)$'s are summed over all the ten subregions, $\sum_e \delta\kappa_{b,e}(x,y) = \Delta\kappa = \delta\kappa_{bFB}$ everywhere.

2.3. Difference measures

One measure of differences between solutions is

$$\delta q_e(x,y,z,t) \equiv q_e(x,y,z,t) - q_{CTL}(x,y,z,t), \tag{5}$$

where q is any model variable and subscript e denotes the test solution from which the variable is taken (FB, EQE, etc.). It is useful to split the temperature anomaly, δT_e, into two components

$$\delta T_e = \delta' T_e + \delta'' T_e, \tag{6}$$

where $\delta' T_e$ results from vertical advection of density ("dynamical" anomaly) and $\delta'' T_e$ from simultaneous temperature and salinity changes in such a way that density remains unchanged ("spiciness" anomaly). See Appendix A for a derivation of (6) and the definitions of $\delta' T_e$ and $\delta'' T_e$. Schneider (2004) and Taguchi and Schneider (2014) provide alternative derivations.

Below the surface mixed layer, each component has a distinct physical interpretation, with $\delta' T_e$ arising primarily from wave adjustments and $\delta'' T_e$ from advection (Section 3.2.3; Appendix A). Within the mixed layer, surface heating and evaporation impact δT_e, and the split between the dynamical and spiciness anomalies is not useful because neither the wave propagation of $\delta' T$ or the advection of $\delta'' T$ is a dominant process (Section 3.3.1).

3. Results

In this section, we first report our control run, comparing modeled and observed fields (Section 3.1). We then provide a general discussion of the adjustment processes by which all of our test experiments reach equilibrium (Section 3.2). Finally, we describe the near-equilibrium (20-year) responses of several of the test solutions in detail (Section 3.3).

3.1. Control run

Fig. 2 shows meridional sections of annual-mean zonal velocity, salinity, and potential density along 160°W from observations and

Please cite this article in press as: Furue, R., et al. Impacts of regional mixing on the temperature structure of the equatorial Pacific Ocean. Part 1: Vertically uniform vertical diffusion. Ocean Modell. (2015), http://dx.doi.org/10.1016/j.ocemod.2014.10.002

from our control run. The maximum speed of the Equatorial Undercurrent (EUC) is about 90 cm s^{-1} in the Johnson et al. (2002) climatology and about 80 cm s^{-1} in the model; moreover, the meridional and vertical extents of the two fields agree well.

The eastward currents at 200–450 m depths and 3–5° from the equator are the northern and southern Tsuchiya jets (TJs; Tsuchiya, 1972, 1975, 1981; McCreary et al., 2002; Furue et al., 2007, 2009). The structures of the model TJs agree fairly well with observations, except that the model has westward currents on the equatorward sides of the TJs. The observed field shows another eastward current just south of the primary one, often termed the secondary Tsuchiya Jet, which is much weaker in the model. Note also that the model has other, vertically-coherent, narrow zonal flows at depths farther from the equator. Eddy-resolving models usually have similar, but stronger, flows, sometimes called "striations" or "zonal jets" (Maximenko et al., 2008), which are thought to be at least partly driven by eddies (e.g., Nakano and Hasumi, 2005; Richards et al., 2006). These flows are much weaker in our model than in typical eddy-resolving models, likely because our mesoscale eddies are much weaker.

There are large-scale bands of high sea-surface salinity between 20°S and 10°S and between 20°N and 30°N (not shown). Waters subducted in these regions flow equatorward in the main pycnocline, forming the tongues of high salinity visible in Fig. 2. Much of this water flows eastward in the EUC, upwells into the mixed layer in the eastern equatorial Pacific, and returns to subtropics near the surface, thereby forming the Pacific's shallow overturning circulation cells, the Subtropical Cells (STCs; McCreary and Lu, 1994). The tongue from the southern hemisphere is more pronounced partly because surface salinity is higher in the southern hemisphere and partly because the subducted water reaches the equator by a more direct path than in the northern hemisphere (Lu and McCreary, 1995). As a result, there is a sharp front of salinity in the pycnocline across the equator. The vertical structure of salinity is complicated near the equator because of this feature especially on the northern side.

Overall, the model salinity field agrees well with the Argo climatology. The most conspicuous difference is that maximum values of salinity are considerably higher than their observed counterparts both in the northern and southern hemispheres. Indeed, the *surface* salinity is much higher in our model than in the Argo climatology (not shown), and it is the subduction of this water that leads to the model's larger subsurface salinities.

3.2. Adjustment processes

All solutions follow similar adjustment processes. They include a very fast, initial response due to interactions of gravity and barotropic waves with eddies (Section 3.2.1), a more gradual diffusive, local response (Section 3.2.2), and slower remote adjustments due to wave propagation and advection (Section 3.2.3).

3.2.1. Fast initial response

Fig. 3 shows δT_{SE} at $z = 150$ m and $t = 300$ days as an example. Even at this early time, alternating positive and negative patches of δT_{SE} exist along 5°N in the eastern Pacific, which is much too far for baroclinic waves to reach from the SE region in only 300 days. Similar chaotic features occur in all other experiments. Furthermore,

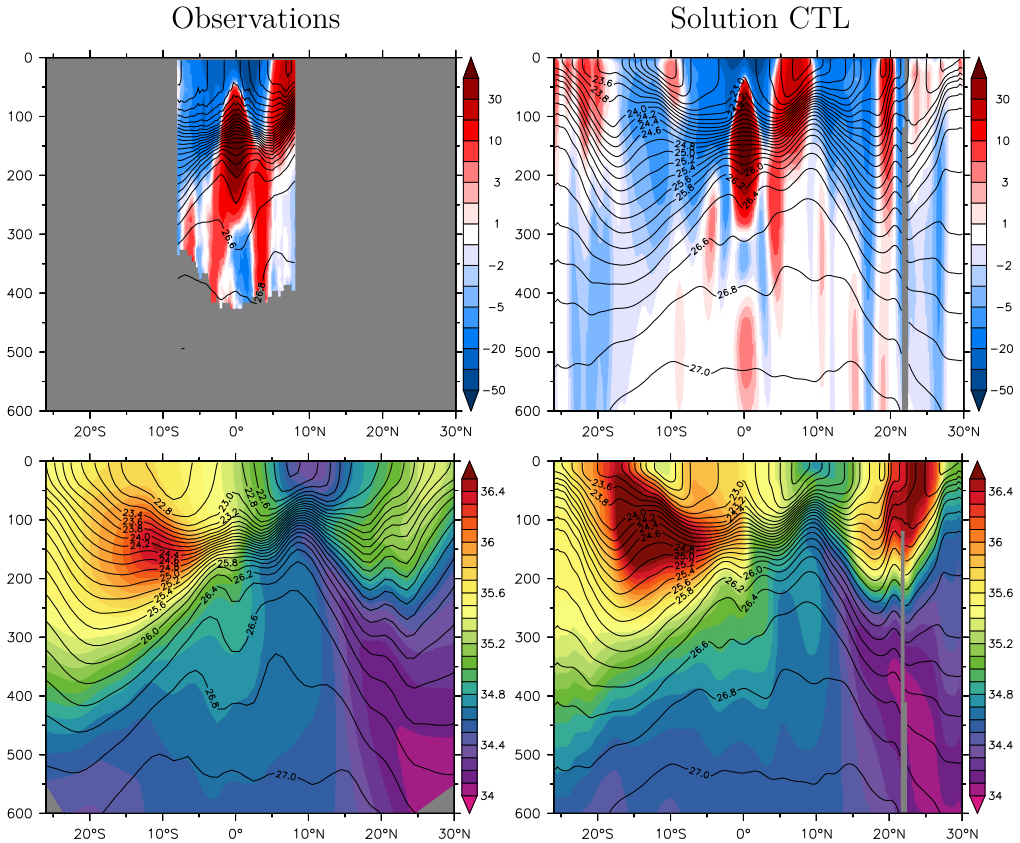

Fig. 2. Sections of zonal velocity and potential density (upper) and salinity and potential density (lower) along 160°W from observations (left) and from the control run (right). The units of velocity, density, and salinity are cm s^{-1}, σ_θ, and psu, respectively. The fields in the top-left panel are from the annual-mean climatology of Johnson et al. (2002) [data available from http://www.pmel.noaa.gov/people/gjohnson/gjohnson.html] and those in the bottom-left panel are from the 2004–2011 RG Argo Climatology (Roemmich and Gilson, 2009) [data available from http://sio-argo.ucsd.edu/RG_Climatology.html]. The modeled fields are averages over year 1 (year 41 of the complete spin up).

Please cite this article in press as: Furue, R., et al. Impacts of regional mixing on the temperature structure of the equatorial Pacific Ocean. Part 1: Vertically uniform vertical diffusion. Ocean Modell. (2015), http://dx.doi.org/10.1016/j.ocemod.2014.10.002

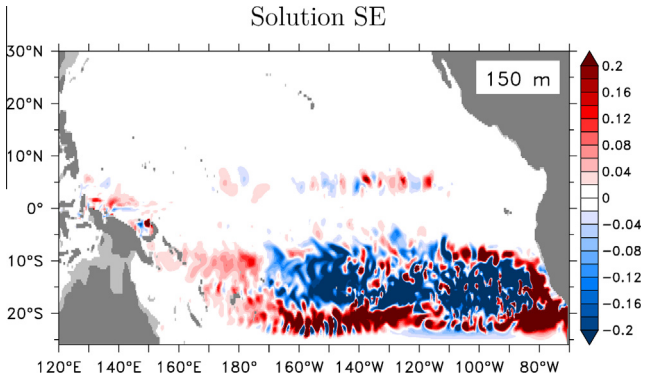

Fig. 3. Map of δT_{SE} at a depth of 150 m after 300 days.

they are not just an initial response, but rather continue throughout the integrations.

The most plausible explanation of this phenomenon is as follows. The sudden change in κ_b in a region generates very fast waves: barotropic and baroclinic gravity waves, and barotropic Rossby and Kelvin waves. Although their amplitudes are small, they are still large enough to perturb mesoscale eddies far from the original region of the κ_b change. Because of the eddies' chaotic nature, their phases are altered appreciably even though their statistical characteristics are hardly affected, resulting in appreciable pointwise differences in field variables between the test run and CTL. As a result, within ~10 days mesoscale anomalies of both signs begin to appear in all dynamical variables (density, velocity, etc.) even in the farthest places from the origin. The amplitudes of these anomalies therefore tend to be large where eddies are strong. For example, the amplitude (as measured by the variance of v near the surface) of Tropical Instability Waves (TIWs) is largest near 5°N in the eastern Pacific, and that is one region where δT_{SE} is large in Fig. 3. To focus on large-scale features, we take temporal averages for the figures below to reduce the amplitudes of these eddy-like anomalies.

Some of the figures below show not only remaining eddy-like anomalies but also front-like structures that are coherent in one spatial direction. A comparison of the test run with the control run suggests that the latter are due to slight shifts in the positions of striations. If the striations are driven by eddies, these shifts may be due to slight changes in eddy statistics, but details are not clear.

3.2.2. Local response

In each experiment, the initial, large-scale response of the temperature and salinity fields to the increased background diffusivity can be described by

$$\delta q_{e,t} \approx \delta \kappa_{b,e}\, q_{0zz}, \tag{7}$$

where q is either temperature or salinity, $q_0 \equiv q_{CTL}$, and the subscripts t and z denote partial derivatives. Eq. (7) follows from the

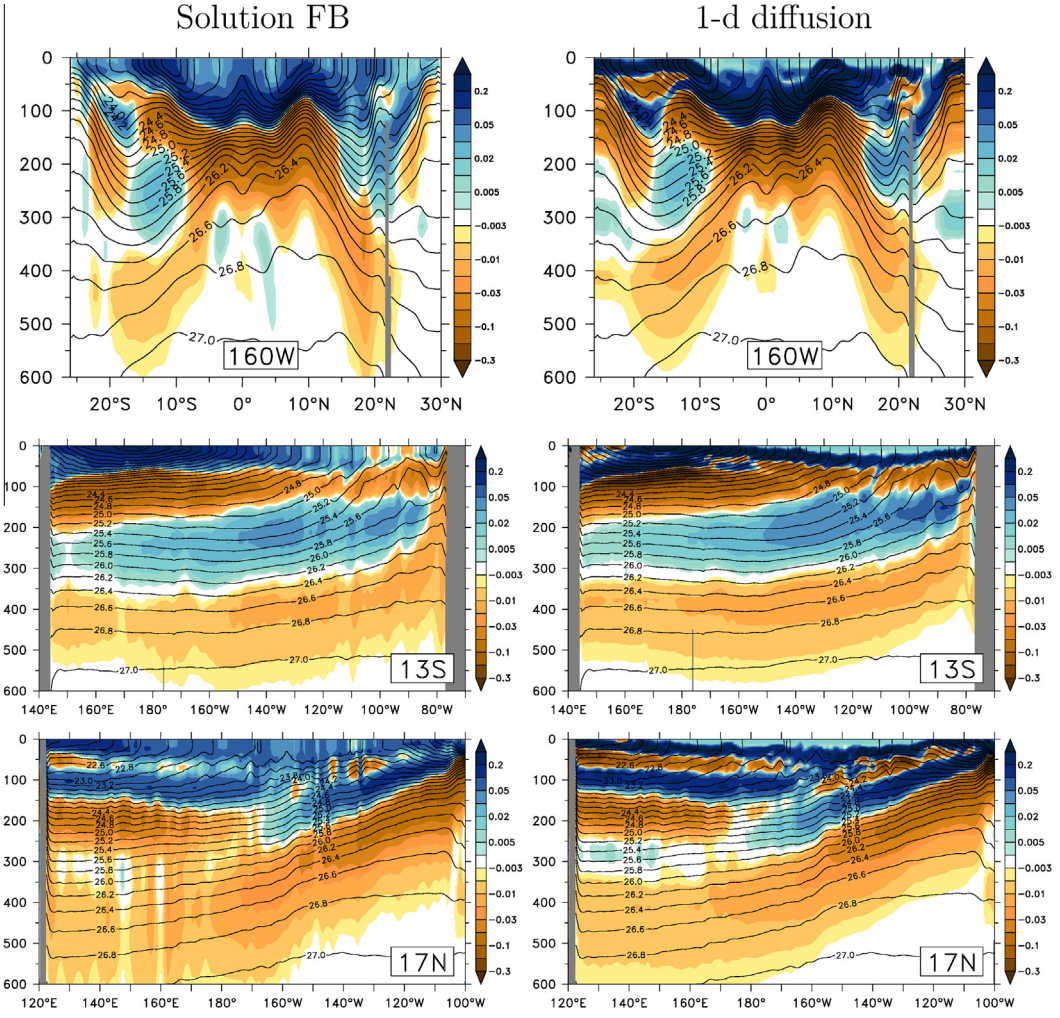

Fig. 4a. Sections of potential-density anomalies for Solution FB along 160°W (top), 13°S (middle), and 17°N (bottom), showing $\bar{\delta}\rho_{FB}$ (left) and $\delta\rho$ computed from one-dimensional diffusion alone (right; see text), where the overbar indicates an average over year 1 (year 41 of the complete spin up).

Please cite this article in press as: Furue, R., et al. Impacts of regional mixing on the temperature structure of the equatorial Pacific Ocean. Part 1: Vertically uniform vertical diffusion. Ocean Modell. (2015), http://dx.doi.org/10.1016/j.ocemod.2014.10.002

temperature or salinity equation that retains only vertical diffusion and assumes that $|\delta\kappa_b q_{0zz}| \gg \max(|\kappa_0 \delta q_{zz}|, |\delta\kappa_b \delta q_{zz}|)$. To assess how well this process explains the early response of a sensitivity experiment, we compute a mean q field that would result from vertical diffusion alone over time Δt, assuming that q_0 is stationary, as

$$\overline{q}_e = q_0 + \overline{\delta} q_e, \quad \overline{\delta} q_e \equiv \delta\kappa_{b,e}\, \overline{q}_{0zz} \times \Delta t/2, \tag{8}$$

where the overbar indicates an average over Δt.

Fig. 4a compares $\overline{\delta}\rho_{FB}$ averaged over year 1 (left panels) with the density anomaly that results from applying (8) to temperature and salinity with $\Delta t = 1$ yr (right panels), showing sections across the equator (top panels), along 13°S (middle panels), and along 17°N (bottom). The large-scale, low-frequency components shown in corresponding left and right panels are similar, indicating that $\delta\rho_{FB}$ is determined primarily by (7). The zeros and signs of $\overline{\delta}\rho_{FB}$ actually tend to coincide with those of $\bar{\rho}_{0zz}$ (not shown) because $\delta\rho \approx -a\delta T + b\delta S$, the vertical gradients of a and b are small, and hence $\delta\rho$ itself approximately obeys (7). Furthermore, the amplitudes in corresponding left and right panels are similar, although the actual anomaly tends to be somewhat weaker than that computed from (8), indicating that the growth of the anomalies has reduced below a linear trend within a year, owing to the onset of the adjustment processes discussed in Section 3.2.3. The exception is within 3° of the southern and northern boundaries where density anomalies are small and the contours of the total density field are nearly horizontal (top panels), a consequence of the restoration of temperature and salinity toward prescribed values in those regions (Section 2.1).

If density depends only on temperature, only on salinity, or if T and S have the same vertical structure (and the vertical gradients of $\partial\rho/\partial T$ and $\partial\rho/\partial S$ are negligible), a diffusion anomaly, $\delta\kappa_b$, will only generate a dynamical anomaly, that is, it will shift isopycnals vertically with no change in spiciness. In the real ocean (and in our control run), however, T and S have different structures, and $\delta\kappa_b$ generates both spiciness and dynamical anomalies (Appendix A). Fig. 4b illustrates the generation of both anomaly types in Solution FB, comparing δT_{FB} (top-left) to its parts due to dynamics $\delta' T_{FB}$ (middle-left) and spiciness $\delta'' T_{FB}$ (bottom-left) during year 1. The pattern of the total temperature anomaly δT_{FB} is very similar to that of $\delta\rho_{FB}$ in Fig. 4a (top-left panel) and it is largely explained by $\delta' T_{FB}$, especially in the tropics. In the subtropics, however, $\delta'' T_{FB}$ is significant because there are prominent salinity signals associated with subsurface waters, namely, high-salinity North Pacific Tropical Water (Tsuchiya, 1968; Suga et al., 2000, and references therein) and South Pacific Subtropical Lower Water (Wyrtki, 1962) overlying deeper, lower-salinity waters (Wyrtki, 1962; Talley, 1985). Fig. 4b also plots temperature anomalies where (7) is assumed to hold individually for both temperature and salinity (right panels). They show that the general patterns of all the anomaly fields in Solution FB are well predicted by the one-dimensional model.

3.2.3. Remote responses

After the initial and local responses, solutions adjust toward a new equilibrium state through wave radiation, advection, and mixing. Locally-forced dynamical anomalies are associated with an unbalanced pressure field that excites baroclinic waves. In contrast, spiciness anomalies do not affect pressure (they are a passive tracer), and hence respond only to advection and mixing. Generally, since the propagation speeds of baroclinic waves are typically faster than advection speeds, remote effects due to baroclinic waves appear sooner than those due to spiciness advection. In a final adjustment, the remote anomalies are also attenuated by diffusion (see Section 3.3.1).

To illustrate dynamical adjustments, Fig. 5 (top panel) shows a longitude-time plot of $\delta' T_{SE}$ at 13°S smoothed in time and in longitude for the 26.6-σ_θ isopycnal surface. This surface lies near the core of the deep negative density anomaly in Solution FB along 13°S east of 167°W (Fig. 4a, middle-left panel). The reversals of the density anomaly in the vertical suggest that Rossby waves associated with several baroclinic modes are locally generated in the SE region.[1] Consistent with this idea, the anomalies in Fig. 5 propagate westward at a speed consistent with first- or second-mode waves. (With a gravity-wave speed of $c \sim 1$–2 m s^{-1}, the phase velocity of long-wavelength Rossby wave is $\beta c^2/f^2 \sim 2$–8 cm s^{-1} at 13°S.) Signals take about 6 years to propagate from the western edge of Region SE (167°E) to the western boundary. The anomaly field has a low-frequency, large-scale response that becomes stationary after about 10 years with interannual oscillation superimposed. The unfiltered field (not shown) includes high-frequency disturbances associated with mesoscale eddies, which are continually generated in the east and propagate westward.

To illustrate spiciness adjustments, Fig. 5 (bottom panel) provides a latitude-time plot of $\delta'' T_{SE}$ on the 24.6-σ_θ isopycnal averaged over 160°–150°W and smoothed in time. Spiciness advects to the equator within the subsurface branch of the South Pacific STC along two primary pathways, one in the far-western ocean and another in the central Pacific (see the discussion in Section 3.3.1). As evident in the plot, the spiciness anomaly first reaches the equator in the central Pacific after about 5 years.

3.3. Regional solutions

Here, we discuss the near-equilibrium (year-20) responses of several of our regional solutions (Solutions SE, NE, EQW, and EQE) that best illustrate of our key findings. Other regional solutions are reported in Appendix B, with the discussions there focusing on differences from the solutions reported here.

3.3.1. Solution SE

Dynamical response. Fig. 6a (top-left panel) illustrates the vertical structure of the near-equilibrium, dynamical response in Region SE, plotting a meridional section of $\delta' T_{SE}$ along 130°W. It is useful to compare the section with that of the initial anomaly along 160°W of Solution FB south of 8°S (Fig. 4b, middle-left panel). (We plot the 160°W section for Solution FB in Figs. 4a and 4b to save space; the section is near the center of the Pacific not too far from the 130°W and 170°E sections shown for the eastern and western experiments, respectively.) In both figures and within the latitude range of the SE region (< 8°S), the dynamical signal is generally positive near and below the bottom of the pycnocline and in the upper pycnocline and it is negative inbetween. This similarity illustrates how much the equilibrium solution is still dominated by 1-d processes. Differences are related mostly to shifts in the position of the density field because the sections are not located at the same longitude; for example, note that near-surface isopycnals are shifted upwards in Solution SE, with $\rho \lesssim 24.0$ σ_θ being absent.

Fig. 6a (top-right panel) shows the near-equilibrium state of $\delta' T_{SE}$ on the 26.6-σ_θ density surface, which lies within the deep positive signal (Fig. 6a, top-left). Within the latitude range of the anomalous mixing ($y < 8$°S), the amplitude of the anomaly is fairly

[1] If the temperature anomaly equation (A.3) and the associated momentum equation are expanded into vertical modes, a set of shallow-water equations is obtained that describes the response of each mode (e.g., McCreary, 1981); in the set, the forcing in the original temperature anomaly equation (the term $\delta\kappa_b T_{0zz}$ on the left-hand side of Eq. 7 or in Eq. A.3) projects onto a mass-source term (Furue et al., 1995). Since the forcing involves several zero crossings (i.e., wherever the curvature of T_0 changes sign) as implied by the spatial pattern of δT (Section 3.2.2), higher-order vertical modes are necessarily part of the overall response.

Please cite this article in press as: Furue, R., et al. Impacts of regional mixing on the temperature structure of the equatorial Pacific Ocean. Part 1: Vertically uniform vertical diffusion. Ocean Modell. (2015), http://dx.doi.org/10.1016/j.ocemod.2014.10.002

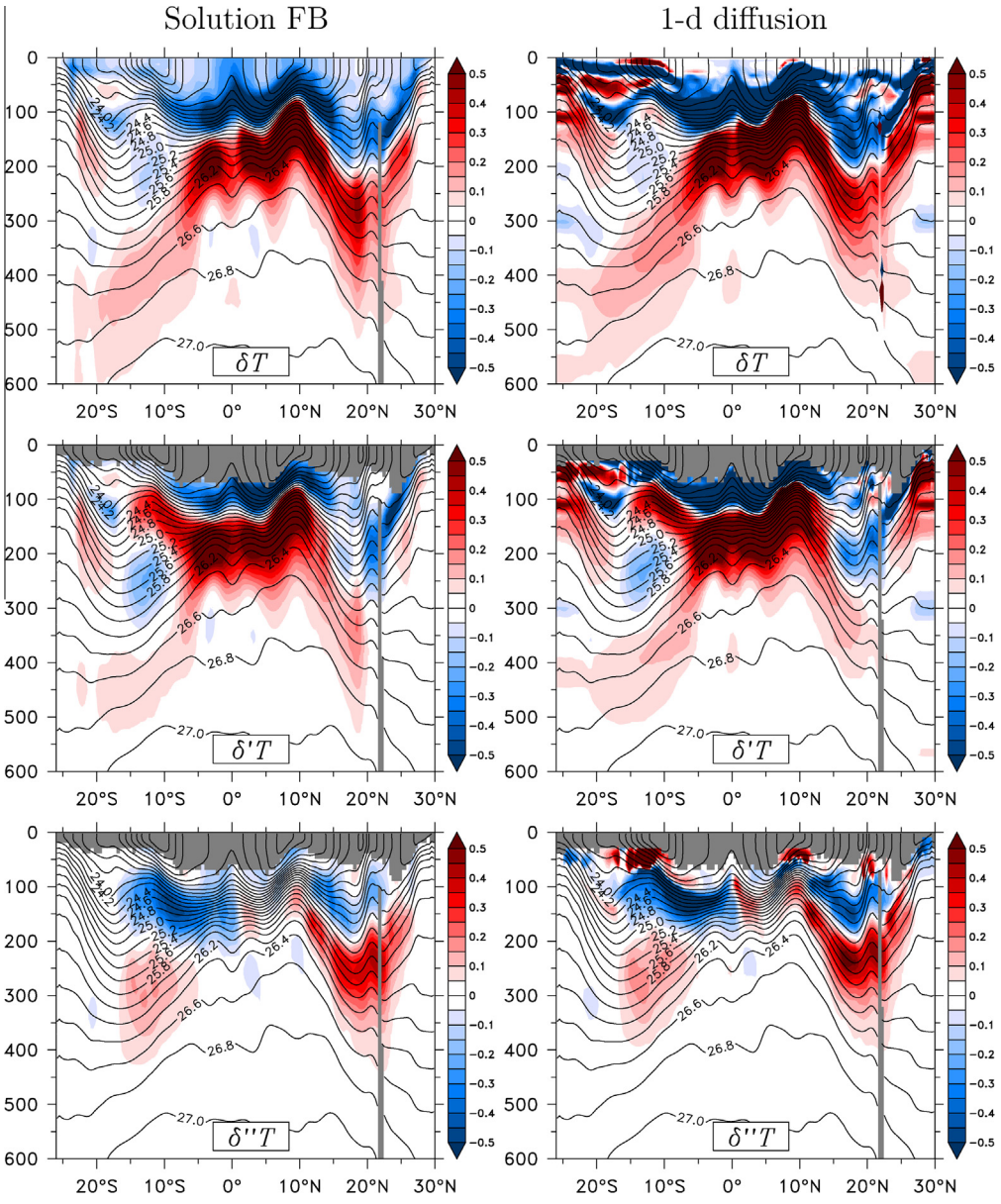

Fig. 4b. Sections of temperature anomalies for Solution FB along 160°W, showing δT_{FB} (top), $\delta' T_{\mathrm{FB}}$ (middle), and $\delta'' T_{\mathrm{FB}}$ (bottom) averaged over year 1 (left), and analogous anomalies determined by assuming that (7) holds for both temperature and salinity (right). Contours show potential density, ρ, from the control solution as a reference. The near-surface gray areas indicate where $\delta' T_{\mathrm{FB}}$ and $\delta'' T_{\mathrm{FB}}$ are undefined because matching isopycnals do not exist in both experiments.

uniform from the western edge of the SE region (167°W) to the western boundary. Near the equator, there is also a weaker signal that broadens to the east, forming a characteristic wedge-shape pattern ($\sim$ 7°S–7°N, 160°W–80°W in the top-right panel of Fig. 6a). (Another part of the remote signal, not visible in the plot, extends into the Indian Ocean through the Indonesian Seas.) On shallower isopycnal surfaces, $\delta' T_{\mathrm{SE}}$ tends to be weaker (except for the mesoscale noise noted earlier) and it is negligible outside the SE latitudinal band (not shown; a very weak version of the response in the top-right panel of Fig. 6a).

The large-scale response in Fig. 6a (top-right panel) is well represented in solutions to a linear, $1\frac{1}{2}$-layer (or equivalently single-mode) shallow-water model forced by an off-equatorial volume source, $\mathcal{Q}(x, y)$, that transfers water into (or out of) the layer (e.g., Anderson, 1976; Kawase, 1987; Spall, 2000). In the latitude band of the forcing, Rossby waves propagate from the forcing region to the western boundary, generating a recirculation that extends across the basin. At the western boundary, part of the flow propagates equatorward as a coastal Kelvin wave and then eastward along the equator as an equatorial Kelvin wave. At the eastern boundary, it propagates first northward and southward along the coast via coastal Kelvin waves and then westward as a packet of long-wavelength Rossby waves. The distinctive bands of $\delta' T_{\mathrm{SE}}$ and $\delta'' T_{\mathrm{SE}}$ within and below the pycnocline north of the equator (Fig. 6a, left panels) are the eddy-like and front-like mesoscale features discussed earlier; it is noteworthy that very similar bands occur in Solutions ESE, ENE, and EQE, suggesting that they are all generated by similar signals from the forcing regions.

The eastern-boundary Rossby waves are attenuated by diapycnal diffusion, with the distance a signal travels depending on the ratio of the wave speed to the timescale of the diffusion. When diffusion is sufficiently strong, the eastern-boundary Rossby waves are damped before they reach the western boundary, and the resulting equilibrium state resembles the wedge-shaped pattern

Please cite this article in press as: Furue, R., et al. Impacts of regional mixing on the temperature structure of the equatorial Pacific Ocean. Part 1: Vertically uniform vertical diffusion. Ocean Modell. (2015), http://dx.doi.org/10.1016/j.ocemod.2014.10.002

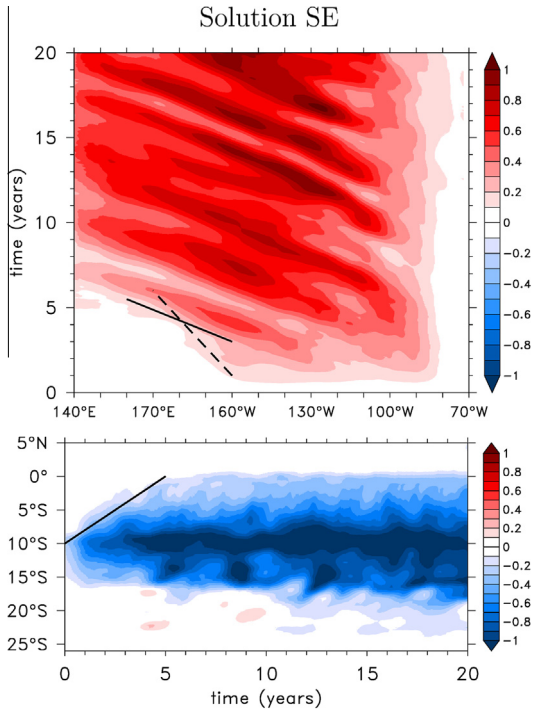

Fig. 5. Longitude-time section of $\delta' T_{SE}$ on the 26.6-σ_θ density surface at 13°S smoothed with a 5° × 0.5 yr two-dimensional moving average (top); time-latitude section of $\delta'' T_{SE}$ on the 24.6-σ_θ density surface averaged over 160°W–150°W smoothed with a 0.5 – yr moving average (bottom). In the top panel, the solid and dashed line segments indicate phase speeds of 80°/5 yr ($\simeq$ 5.5 cm s^{-1}) and 30°/5 yr ($\simeq$ 2 cm s^{-1}); and in the lower panel, the solid line segment indicates a phase speed of 10°/5 yr ($\simeq$ 0.7 cm s^{-1})

in Fig. 6a (McCreary, 1981; Kawase, 1987). An alternative explanation for the wedge shape is that it represents the pathways of higher-order vertical-mode ($n \geqslant 2$) Rossby waves emanating from the eastern boundary, which are bent equatorward by the background Sverdrup circulation (Luyten and Stommel, 1986; McCreary et al., 2002; Furue et al., 2007, 2009). Consistent with this idea, the poleward edge of the positive $\delta' T_{SE}$ signal farther west is tilted somewhat equatorward (top-right panel of Fig. 6a). It is difficult to determine which process dominates unless the vertical-modal structure of $\delta' T$ and the strength of diffusive attenuation on each vertical mode are quantitatively known.

Spiciness response. Fig. 6a (bottom-left panel) plots a meridional section of $\delta'' T_{SE}$. As for $\delta' T_{SE}$, it is similar to the initial 1-d response in Solution FB south of 8°S (Fig. 4b, bottom-left panel), except shifted vertically somewhat due to zonal changes in the background temperature and salinity fields and extending to somewhat deeper depths as time passes. Note that the shallow negative anomaly extends equatorward, whereas the deep positive one does not, the extension resulting from equatorward advection within the subsurface branch of the South Pacific STC, as discussed next.

Fig. 6a (bottom-right panel) plots $\delta'' T_{SE}$ on the 24.6-σ_θ surface. It is located near the middle of the aforementioned negative spiciness signal, lies within the subsurface salinity tongue that extends from the subtropics to the equator (Fig. 2), and outcrops within the SE region (light-gray shading in the bottom-right panel of Fig. 6a). The locally-generated $\delta'' T_{SE}$ signal is advected westward of 160°W by the South Pacific Subtropical Gyre and equatorward of 10°S within the South Pacific STC following two primary pathways: one that extends to the western boundary near 5°S, and another that intersects the equator in mid-basin, as indicated by the geostrophic streamfunction (contours).

The $\delta'' T_{SE}$ signal in the western-boundary pathway flows toward the equator in the western-boundary current and then eastward in the EUC. Note that part of this signal flows into the Indonesian Seas, but most of it retroflects to join the EUC with little continuing southward into the Banda Sea (Fig. 1). This retroflection is consistent with theoretical and modeling results, which show that almost all the ITF within the upper 400 m arises from the North Pacific (Section 3.3.2).

Since part of the western-boundary current crosses the equator (Godfrey et al., 1993; Kashino et al., 1996) before flowing into the EUC, $\delta'' T_{SE}$ exists on both sides of the equator in the western ocean. This feature is barely visible in Fig. 6a and is confirmed by examining meridional sections of $\delta'' T_{SE}$ at various longitudes (not shown). In contrast, the $\delta'' T_{SE}$ signal that follows the interior pathway does not cross the equator, and flows eastward only on the southern side of the EUC. Near South America, the $\delta'' T_{SE}$ signal is likely due to southward advection from the EUC; the background mean flow is generally southward in this density range between 94°E and the coast and between the equator and 8°S, including the strong Peruvian Coastal Undercurrent (not shown; Lukas, 1986; Penven et al., 2005; Montes et al., 2010).

A comparison of the two right panels of Fig. 6a illustrates the striking differences that can occur in the propagation of dynamical ($\delta' T_{SE}$) and spiciness ($\delta'' T_{SE}$) signals, in this case with the spiciness signal extending more prominently equatorward. Similar differences occur in our other regional solutions, and have been noted previously by Nonaka and Xie (2000) and Taguchi and Schneider (2014).

Equatorial response. Fig. 6b illustrates the vertical structures of the dynamic and spiciness anomalies along the equator, plotting δT_{SE}, $\delta' T_{SE}$, and $\delta'' T_{SE}$ fields averaged from 1°S to 1°N. Consistent with Fig. 6a (top panels), the deep dynamical signal $\delta' T_{SE}$ (Fig. 6b, middle panel) is spread throughout the equatorial ocean. There is also a near-surface, positive anomaly that is locally generated (see below). It is noteworthy that $\delta' T_{SE}$ has fewer zero crossings at the equator than it does in the forcing region (Fig. 4b, middle-left panel south of 8°S), an indication that either Rossby waves associated with higher-order vertical modes are preferentially damped or the large change in stratification modifies the structure of the modes. Also consistent with Fig. 6a, there is a strong, negative spiciness signal $\delta'' T_{SE}$ within the pycnocline (Fig. 6b, bottom panel), which is advected to the equator from Region SE along the two pathways noted above. Below the pycnocline, there is a positive anomaly (bottom panel) near the western boundary. Most of it flows out of the basin as a deep part of the ITF (not shown; e.g., McCreary et al., 2007), with some bending eastward to join the southern Tsuchiya Jet and the lower part of the EUC.

There are also negative $\delta'' T_{SE}$ and positive $\delta' T_{SE}$ signals above the pycnocline. Because of surface fluxes, however, these signals cannot be interpreted as arising solely from the remote forcing region. The negative $\delta'' T_{SE}$ signal is advected along the equator within the pycnocline by the EUC and is mixed upward into the surface layer in the eastern Pacific. The heat flux into the ocean is increased there, reducing the negative temperature anomaly (Fig. 6b, top panel) and leaving behind a negative salinity anomaly. At the same time, evaporation is reduced owing to the lower SST while precipitation is not affected (Section 2.1), enhancing the negative salinity anomaly. This anomaly is advected westward by the surface South Equatorial Current while the negative temperature anomaly is almost erased by the surface heating before reaching the western Pacific. Since the dominance of negative salinity anomaly implies a negative density anomaly in the western Pacific, the vanishing temperature anomaly there is projected onto $\delta' T > 0$ (see Eq. A.2c), resulting in $\delta'' T < 0$ since $\delta T = \delta' T + \delta'' T$. The positive $\delta' T$ and negative $\delta'' T$ responses near the surface in the western Pacific are locally generated in this way, and so the former (latter) is not indicative of wave radiation (advection) from Region SE. A similar issue occurs in all the other solutions.

Please cite this article in press as: Furue, R., et al. Impacts of regional mixing on the temperature structure of the equatorial Pacific Ocean. Part 1: Vertically uniform vertical diffusion. Ocean Modell. (2015), http://dx.doi.org/10.1016/j.ocemod.2014.10.002

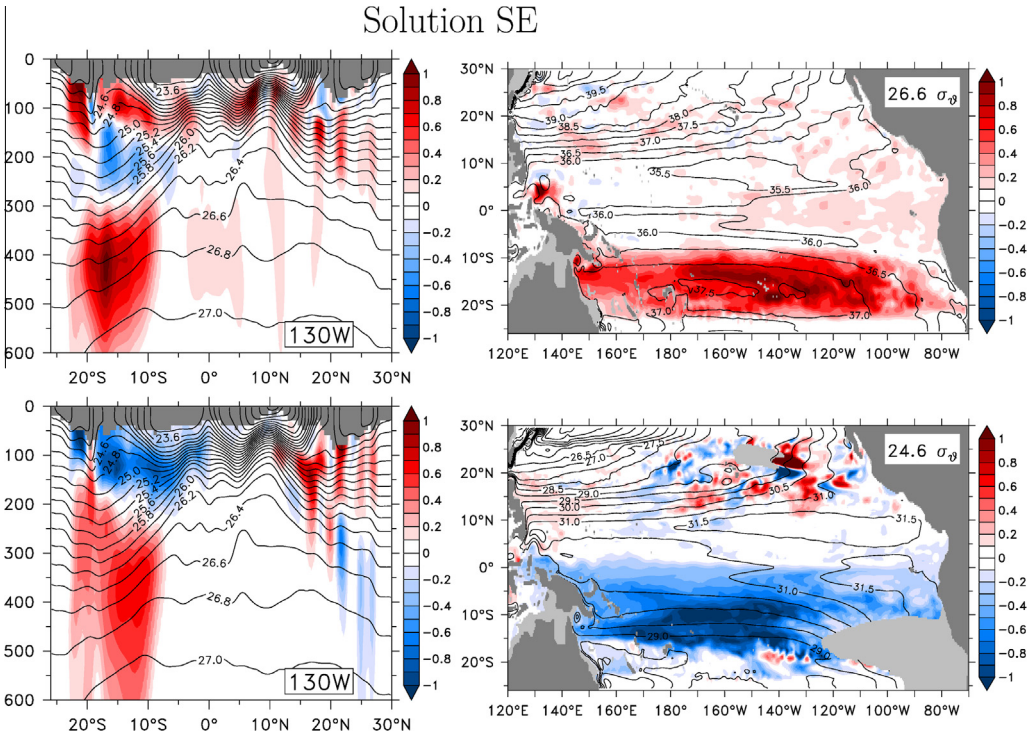

Fig. 6a. Meridional sections along 130°W (left) and maps on density surfaces (right) of temperature differences (color shading, °C) and density (contours on left panels, σ_θ) or Montgomery streamfunction (contours on right panels, $m^2\ s^{-2}$) averaged during year 20. The sections show $\delta' T_{SE}$ (top-left), $\delta'' T_{SE}$ (bottom-left), and ρ_{CTL}. The maps plot $\delta' T_{SE}$ on the 26.6-σ_θ density surface (top-right), $\delta'' T_{SE}$ on the 24.6-σ_θ density surface (bottom-right), and the Montgomery function from CTL, which is defined here as $m = -(p + \rho g z)/\rho_0$ and $\rho_0 = 1024\ kg\ m^{-3}$ is a constant reference density.

3.3.2. Solution NE

Dynamical response. The local and remote responses in Solution NE differ considerably from those in Solution SE, a consequence of differences in the background velocity, temperature, and salinity fields between the northern and southern hemispheres.

Fig. 7a (top-left panel) illustrates the vertical structure of the near-equilibrium, dynamical response in Solution NE along 130°W. As for Solution SE, the response is similar to that of the initial anomaly of Solution FB north of 8°N (not shown), indicating that the solution is dominated by 1-d mixing in the forcing region. The local response is considerably different from that for Solution SE (Fig. 6a, top-left panel), however, a consequence of the more complicated background density field in the northern-hemisphere tropics.

Fig. 7a (top-right panel) shows the near-equilibrium state of $\delta' T_{NE}$ on the 26.6-σ_θ density surface. As for Solution SE (top-right panel of Fig. 6a), the response is confined largely within the latitude band of Region NE, except that anomalies appear to tilt somewhat equatorward to the west probably owing to the propagation of higher-order, baroclinic Rossby waves being affected by the background flow. Wave propagation also ensures that weak deepening (red) spreads throughout the rest of the ocean, analogous to the near-equatorial deepening on the 26.6-σ_θ surface in Solution SE (Fig. 6a). Interestingly, the band of negative (blue) $\delta' T_{NE}$ in the eastern ocean does not propagate out of the forcing region, because it is erased by forcing (Eq. 7) of the opposite sign before it can do so.

Spiciness response. Fig. 7a (bottom-left panel) plots a meridional section of $\delta'' T_{NE}$. As for $\delta' T_{SE}$, it is determined largely by 1-d processes in the forcing region, and it differs markedly from $\delta'' T_{SE}$ because of the different stratifications in the two regions (see below).

Fig. 7a (bottom-right panel) shows the near-equilibrium state of $\delta'' T_{NE}$ on the 24.6-σ_θ density surface. From the bottom-left panel, we can see that it is only in this depth range that the signal is advected to the equator, and it does so within the subsurface branch of the North Pacific STC, which lacks a strong interior pathway due to the presence of the NECC (Lu and McCreary, 1995). In contrast to Solution SE, then, $\delta'' T_{NE}$ flows to the western boundary within the North Equatorial Current and then equatorward in the southward-flowing branch of the Philippine Current. At the southern tip of the Philippines, part of that current retroflects to flow eastward in the North Equatorial Countercurrent (NECC; ~6°N) and along the northern flank of the EUC (Nonaka and Xie, 2000), this western boundary current not flowing across the equator unlike the southern-hemisphere counterpart. Another part turns west to flow across the Sulawesi Sea (Fig. 1), then south through the Makassar Strait (located just west of the western edge of the plot in Fig. 7a; see Fig. 1), and finally east into the Banda Sea, a circulation in the Indonesian Seas that complements that of Solution SE (compare bottom-right panels of Figs. 7a and 6a) and is consistent with observations and models (e.g., McCreary et al., 2007).

Within the forcing region, there is a patch of large positive (red) $\delta'' T_{NE}$ values (Fig. 7a, bottom panels), with no counterpart in Solution SE (Fig. 6a, bottom panels). The difference comes from the very different water-mass structures between the northern and southern tropical regions (Fig. 2, lower panels); for example, the salinity-minimum water is much shallower in the northern hemisphere. As with the negative band of $\delta' T_{SE}$, the positive $\delta'' T_{NE}$ patch does not extend west of Region NE because it is eliminated by forcing of the opposite sign.

There is also a distinctive negative (blue) $\delta'' T_{NE}$ patch just west of the outcropping. It emerges only after several years of integration, indicating that it does not result from 1-d forcing. The 24.6-σ_θ surface lies just beneath the surface mixed layer in this region, and sea-surface salinity anomaly there generally has a spatial pattern similar to that of $\delta'' T_{NE}$ (not shown). These properties suggest that the blue patch results from gradual changes in mixed-layer properties, but details of this adjustment are not clear.

Please cite this article in press as: Furue, R., et al. Impacts of regional mixing on the temperature structure of the equatorial Pacific Ocean. Part 1: Vertically uniform vertical diffusion. Ocean Modell. (2015), http://dx.doi.org/10.1016/j.ocemod.2014.10.002

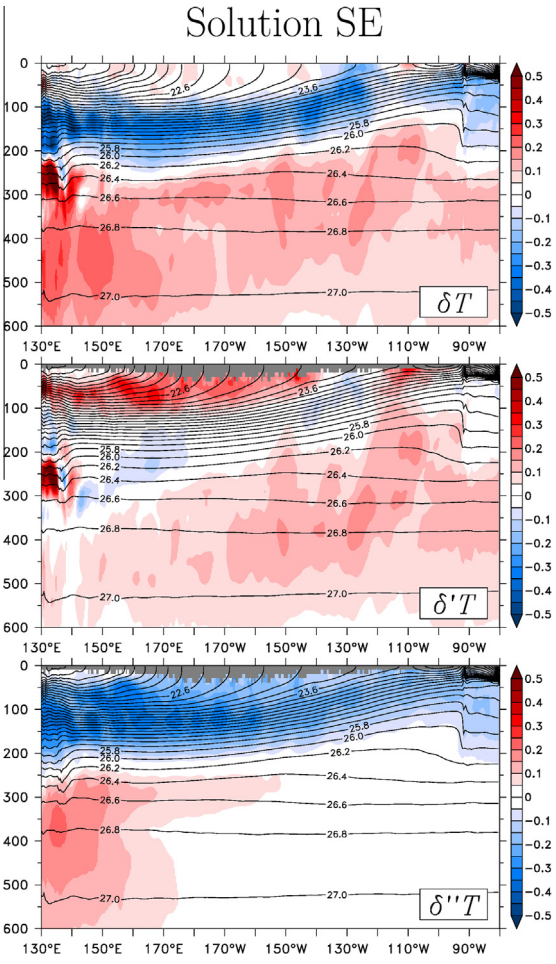

Fig. 6b. Zonal sections of temperature differences (color shading, °C), showing δT_{SE} (top), $\delta' T_{\mathrm{SE}}$ (middle), $\delta'' T_{\mathrm{SE}}$ (bottom), and ρ_{CTL} (σ_θ) averaged from 1°S–1°N and during year 20.

Equatorial response. Fig. 7b plots $\delta T_{\mathrm{NE}}, \delta' T_{\mathrm{NE}}$, and $\delta'' T_{\mathrm{NE}}$ along the equator averaged from 1°S to 1°N. Consistent with the top panels of Fig. 7a, the deep dynamical signal $\delta' T_{\mathrm{NE}}$ (Fig. 7b, middle panel) extends across the equatorial ocean. There is also a shallower positive signal centered about 25 σ_θ, due to the strong, locally-forced anomaly in this density band (top-left panel of Fig. 7a). Consistent with the bottom panels of Fig. 7a, there is only a weak spiciness signal $\delta'' T_{\mathrm{NE}}$ within the pycnocline (bottom panel of Fig. 7b). It is much weaker than in Solution SE, because the subsurface branch of the North Pacific STC lacks a central-Pacific pathway, part of the anomaly flows into the NECC, part exits the basin via the ITF, and the signal is weakened by the 1°S–1°N averaging since it is present only on the northern flank of the EUC.

3.3.3. Solutions EQW and EQE

In contrast to the other experiments, the locally-generated $\delta' T_{\mathrm{EQW}}$ anomaly projects onto the equatorial Kelvin wave and only a few, low-horizontal-mode, Rossby waves. As a consequence, the locally-forced pattern of $\delta' T_{\mathrm{EQW}}$ spreads meridionally as far as $y \sim \pm 4°$ within a year. The amplitude of $\delta' T_{\mathrm{EQW}}$ is much smaller during year 1 than that from the 1-d calculation (not shown, but barely visible by comparing left- and right-middle panels of Fig. 4b), although the spatial pattern of $\delta' T_{\mathrm{EQW}}$ agrees well with the 1-d calculation, consistent with the fact that equatorial waves are much faster than off-equatorial and tropical Rossby waves. It is hard to establish which vertical modes are predominant because of the strong mesoscale noise, but it is clear that positive (negative) $\delta' T_{\mathrm{EQW}}$ below (above) the center of the pycnocline immediately propagates eastward as an equatorial Kelvin wave. The upper negative signal vanishes as it reaches the mixed layer in the east (Fig. 8b, middle-left), but the lower positive signal propagates poleward along the coasts of North and South America as coastal Kelvin waves (Fig. 8a, upper-right). Interestingly, in the near-equilibrium state the maximum response in the pycnocline is not located on the equator but at about 7°N and 140°–130°W (Fig. 8a, upper-right). This anomaly is very similar to the one in Solutions SE (Fig. 6a, upper-left, ~7°N and ~90m) and ESE (Fig. B.3a, upper panels), suggesting that both result from the same process, that is, the reflection of Rossby waves from the eastern boundary.

Within the pycnocline, $\delta'' T_{\mathrm{EQW}}$ is much stronger in the southern hemisphere (Fig. 8a, lower-left), and is reasonably consistent with the 1-d calculation (not shown), possibly reflecting the salinity contrast across the equator (Fig. 2). This signal is advected eastward in the EUC, forming a tongue much narrower than the width of the dynamical signal (Fig. 8a, lower-right).

Along the equator (Fig. 8b, left panels), the positive temperature anomaly δT_{EQW} in the lower pycnocline is due to the dynamical signal $\delta' T_{\mathrm{EQW}}$ partly canceled by the negative $\delta'' T_{\mathrm{EQW}}$ signal. The strong negative δT_{EQW} signal in the upper pycnocline is a superposition of $\delta'' T_{\mathrm{EQW}}$ and the directly-forced negative $\delta' T_{\mathrm{EQW}}$. The deeper positive anomaly is due to spiciness.

The properties of both dynamical and spiciness anomalies in Solution EQE are similar to those of Solution EQW. In contrast to Solution EQW, the positive $\delta' T_{\mathrm{EQW}}$ signal in the pycnocline does not extend below the pycnocline (Compare the middle-right and middle-left panels of Fig. 8b). The locally-generated spiciness anomaly $\delta'' T_{\mathrm{EQE}}$ is much weaker than the dynamical one (middle-right and lower-right panels of Fig. 8b) and does not agree with the 1-d calculation during year 1 (not shown). This weak signal is likely generated by $\delta \boldsymbol{u}$ due to the dynamical response (Appendix A.3). In the pycnocline, it is then advected eastward by the EUC and spreads southward near the eastern coast (not shown).

Along the equator, the positive temperature anomaly δT_{EQE} within the pycnocline and the weaker negative band just below it are due to the dynamical signal $\delta' T_{\mathrm{EQE}}$ (Fig. 8b), except $\delta'' T_{\mathrm{EQE}}$ dominates in the far east below the pycnocline. The deeper positive anomaly is due to spiciness. The patch of the directly-forced negative $\delta' T_{\mathrm{EQE}}$ in the upper pycnocline is visible east of ~160°W.

3.3.4. Tropical SST

Fig. 9 illustrates the impact of regional κ_{b} anomalies on the average temperature of the upper 50 m ($\mathcal{T}$) during year 20, showing $\mathcal{T}$ anomalies ($\delta\mathcal{T}$) for Experiment FB (top-left) and seven of the regional experiments. In Experiment FB (top-left panel), $\mathcal{T}$ is generally lower by 0.2–0.8°C throughout the tropics, except for the strong localized warmings off the Central America and Baja California and the weak warming in the southeastern Pacific. In the regional experiments, locally-generated $\delta\mathcal{T}$'s tend to be dominated by negative signals because T_{0zz} tends to be negative above the pycnocline (Section 3.2.2; Fig. 4b). As discussed above, the locally generated signals converge to the equator and propagate eastward along it. In the eastern-equatorial Pacific (EEPO), the pycnocline rises near the surface so that upper-pycnocline water impacts $\mathcal{T}$ there. Therefore, the part of the remotely-generated signals that impact $\delta\mathcal{T}$ in the EEPO are those that lie on the upper pycnocline. As a single measure of the impact of $\delta\kappa_{\mathrm{b}}$ in the EEPO, we use $\delta\mathcal{T}$ averaged over the Niño-3 region ($\delta\mathcal{T}_{\mathrm{N3}}$; 150°W–90°W, 5°S–5°N). For solution FB, $\delta\mathcal{T}_{\mathrm{N3}} = -0.35$°C.

Individual contributions of the regional solutions to equatorial $\delta\mathcal{T}$ differ considerably, owing to the different, local, background temperature and salinity structures that generate them and their different ways of propagation. The largest contributions to

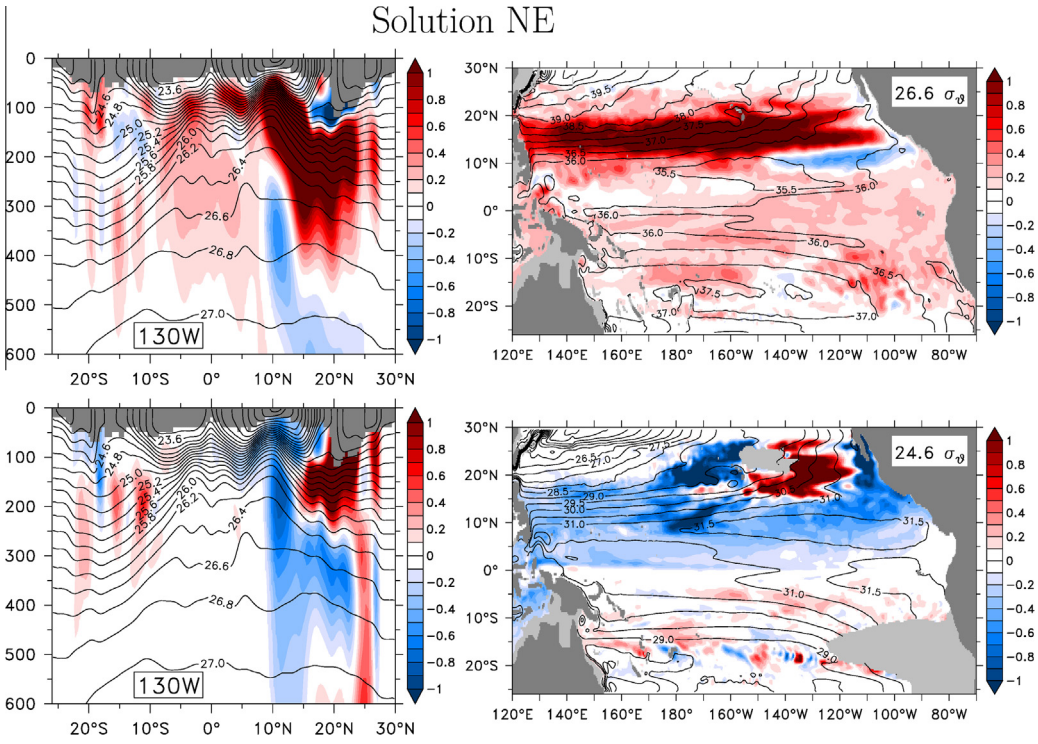

Fig. 7a. Same as Fig. 6a but for Solution NE.

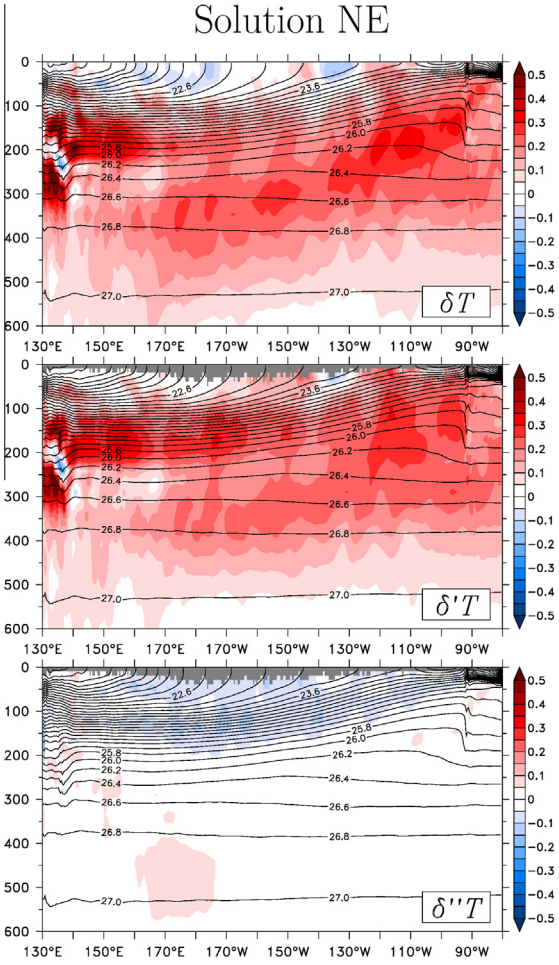

Fig. 7b. Same as Fig. 6b but for Solution NE.

negative $\delta\mathcal{T}_{N3}$ come from Solutions ESE and ENE (bottom and upper-middle right panels of Fig. 9), a consequence of their forcing regions having the largest overlap with the Niño-3 region. Interestingly, negative contributions from Solution EQE and EQW are much smaller, because the locally forced negative anomaly is balanced by the underlying, positive one that rises into the upper 50 m there (Fig. 8b). The contributions from Solutions ESW and ENW (bottom and upper-middle left panels of Fig. 9) are small because their near-surface, negative dynamical signals do not much propagate to the eastern equatorial Pacific, and their positive dynamical signals partially cancel their negative spiciness signals (right panels of Figs. B.3b and B.4b). In Solutions NE (top-right panel of Fig. 9) and NW (not shown), there is a systematic *warming* of $\mathcal{T}$ in the EEPO, a consequence of the dynamical, warming signal rising to the surface there (Figs. 7b and B.2b). In contrast, in Solutions SE and SW (not shown) $\delta\mathcal{T}$ in the EEPO is weak because their positive dynamical signal is balanced by a strong negative spiciness signal (Figs. 6b and B.1b). The contribution from Solution SE is weakly negative because the negative spiciness signal dominates, and that from SW is weakly positive because the spiciness is somewhat weaker and dynamical signal is somewhat stronger (Appendix B.1).

It was surprising to us that the contributions to equatorial $\mathcal{T}$ differ so much among the regional solutions, and that altogether they tend to cool, rather than warm, $\mathcal{T}$ in the EEPO. It was therefore also surprising to find in the second part of our study that this result changes markedly when the depth range of the κ_b anomalies is limited above the mid-pycnocline depth, in which case *all* the regional solutions cause $\mathcal{T}$ warming in the EEPO (Jia et al., 2014).

4. Summary and discussion

4.1. Summary

In this paper, we investigate the sensitivity of solutions to regional changes in vertical diffusion. Specifically, we vary the background diffusion coefficient, κ_b, within spatially distinct subregions of the tropical Pacific (Fig. 1 and Table 1), assess the

Please cite this article in press as: Furue, R., et al. Impacts of regional mixing on the temperature structure of the equatorial Pacific Ocean. Part 1: Vertically uniform vertical diffusion. Ocean Modell. (2015), http://dx.doi.org/10.1016/j.ocemod.2014.10.002

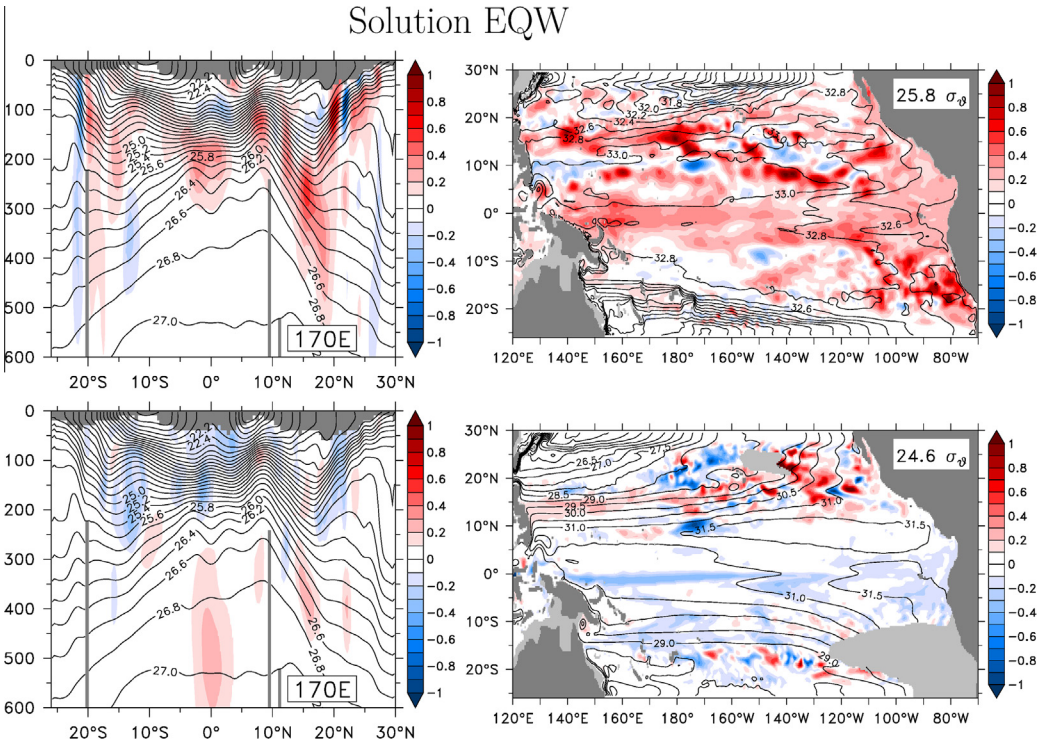

Fig. 8a. Same as Fig. 6a but for Solution EQW and for the 25.8-σ_θ surface (upper-right).

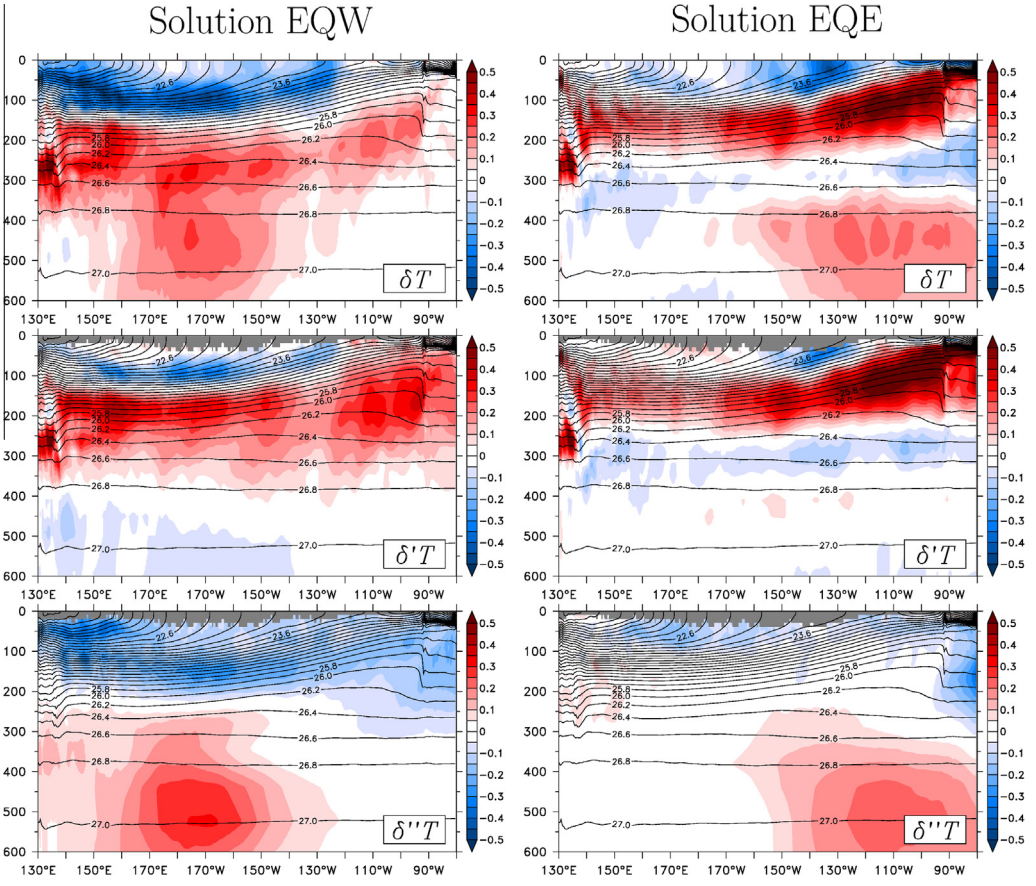

Fig. 8b. Same as Fig. 6b but for Solutions EQE (left) and EQW (right).

Please cite this article in press as: Furue, R., et al. Impacts of regional mixing on the temperature structure of the equatorial Pacific Ocean. Part 1: Vertically uniform vertical diffusion. Ocean Modell. (2015), http://dx.doi.org/10.1016/j.ocemod.2014.10.002

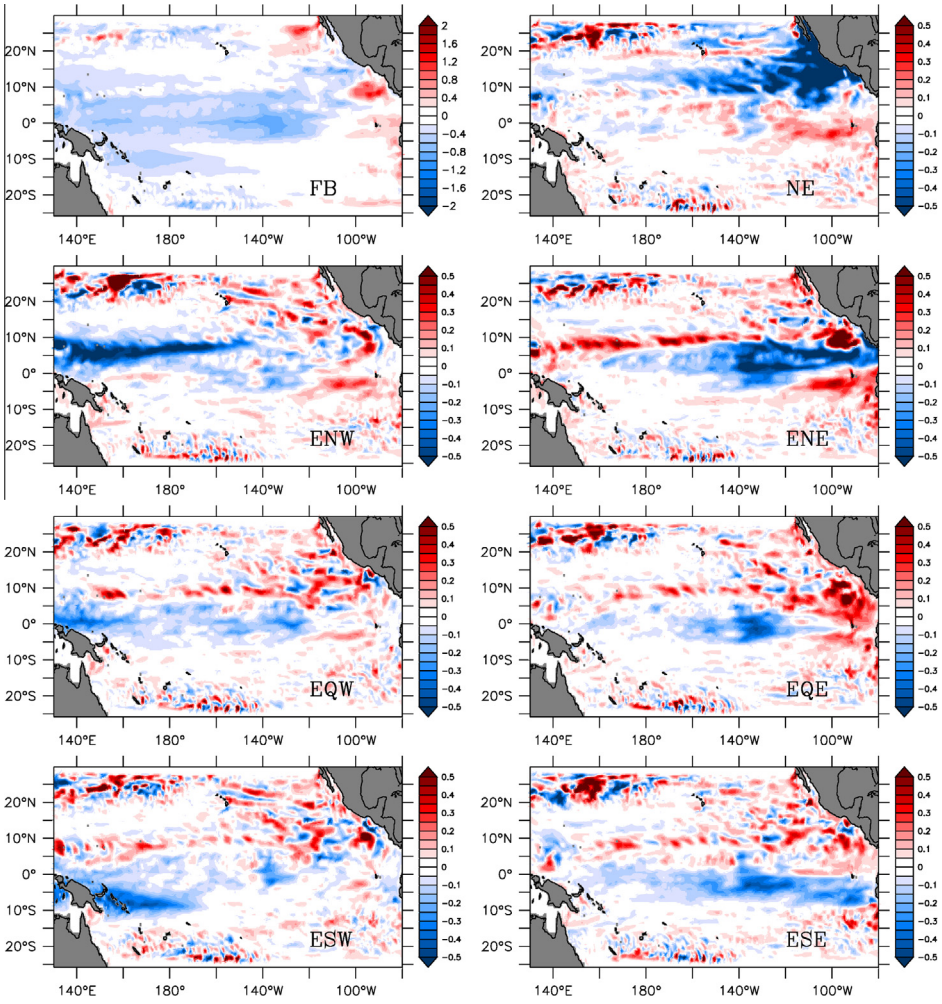

Fig. 9. Maps of near-surface (average in the upper 50 m) temperature anomalies (°C) during year 20 for various experiments. Notice the change in color scale for Solution FB.

impacts of those changes, and diagnose the processes that account for them.

Solutions respond to $\delta\kappa_b$ in three ways. Initially, there is a fast response (several months), due to the interaction of rapidly-propagating, barotropic and gravity waves with eddies and other mesoscale features (Fig. 3). It is followed by a local response (roughly one year) determined by 1-d (vertical) diffusion (Eq. 7; Figs. 4a and 4b). At this stage, temperature and salinity anomalies are generated that are either associated with (dynamical anomalies) or without (spiciness anomalies) a density change. In a final adjustment stage, the dynamical and spiciness anomalies spread to remote regions by radiation of Rossby and Kelvin waves and by advection, respectively (Section 3.2.3). Velocity anomalies due to dynamical signals can generate secondary spiciness anomalies along the equator (Appendix A.3).

In near-equilibrium solutions, the response within the forcing region is not much different from the 1-d response (Section 3.3). Dynamical anomalies generated in the tropical (Regions SE, SW, NE, and NW) and off-equatorial regions (ESE, EWE, ENE, and ENW) propagate to the western boundary (Fig. 10a), generating a recirculation that extends from the forcing region to the western boundary; as a result, dynamical anomalies are generally much larger in the latitude band of the forcing. At the western boundary, part of the flow propagates equatorward as a coastal Kelvin wave and then eastward along the equator as an equatorial Kelvin wave. At the eastern boundary, it propagates first northward and southward along the coast via coastal Kelvin waves and then westward as a packet of long-wavelength Rossby waves. When the forcing lies on the equator (Experiments EQW and EQE), equatorial Kelvin waves are directly generated.

Spiciness anomalies spread equatorward within the pycnocline (Fig. 10b), where they are carried to the equator as part of the subsurface branch of the Pacific Subtropical Cells (STCs), and spiciness also extends to the equator via western-boundary currents. Spiciness anomalies from the northern hemisphere (NH) tend to be weaker along the equator than those from the southern hemisphere (SH), because the subsurface branch of the North Pacific STC lacks a central-Pacific pathway, part of the anomaly flows into the NECC, part exits the basin via the Indonesian Throughflow, and the western boundary current in the NH is blocked by the flow from the SH. [We note that the various pathways of spiciness anomalies have implications for natural variability in subsurface salinity and potentially for SST through mixing or upwelling. For example, the pathway from the tropical North Pacific in our Experiments NE and NW suggests that spiciness anomalies can enter the Indonesian Seas. Since there is strong vertical mixing in the Indonesian Seas, such subsurface spiciness signals may impact SST there (Ffield and Gordon, 1992; Ffield and Gordon, 1996).]

Below the mixed layer, temperature anomalies along the equator are a superposition of dynamical and spiciness components. Their structure generally depends on the strength and spatial patterns of the signals in the regions where they are locally generated and on the processes by which they spread to the equator. Forcing near and at the equator (Regions ESE, ESW, ENE, ENW, EQE, and

Please cite this article in press as: Furue, R., et al. Impacts of regional mixing on the temperature structure of the equatorial Pacific Ocean. Part 1: Vertically uniform vertical diffusion. Ocean Modell. (2015), http://dx.doi.org/10.1016/j.ocemod.2014.10.002

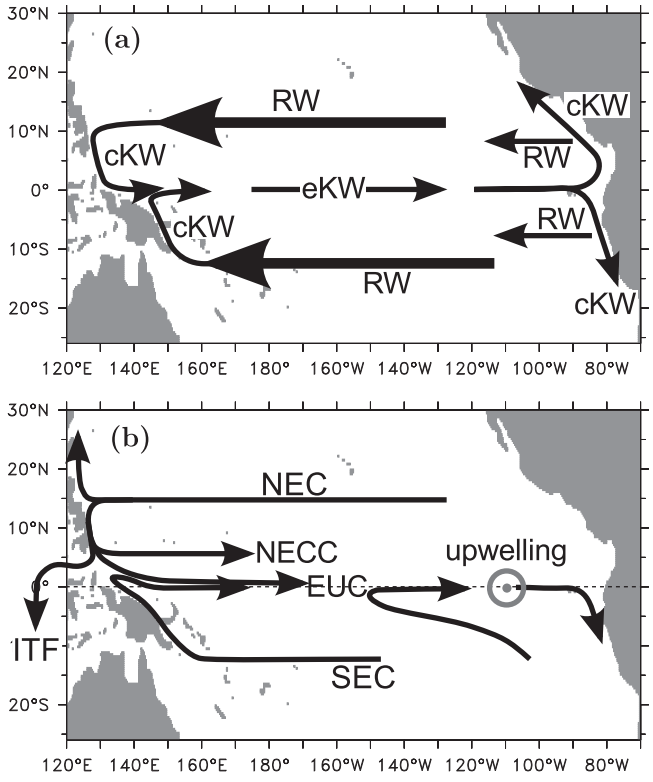

Fig. 10. Schematic diagrams summarizing the main pathways of (a) dynamical signal (b) spiciness anomalies. Labels RW, cKW, and eKW stand for Rossby waves, coastal Kelvin waves, and equatorial Kelvin waves, respectively. The spiciness pathways are shown at pycnocline depths.

EQW), however, has common influences on the equatorial temperature structure. It generates positive dynamical anomalies (deepening of isopycnals) in the lower pycnocline and weaker negative dynamical anomalies in the upper pycnocline; it also generates negative spiciness anomalies in the pycnocline, which partially cancel the positive anomalies due to dynamical signals in the lower pycnocline (Figs. 8b, B.3b, and B.4b).

4.2. Discussion

4.2.1. Linearity

An assumption underlying our split of the domain into subregions is that the ocean's response to $\delta\kappa_b$ is (approximately) linear, that is, the total response is close to the sum of the individual responses. Linearity should hold in the limit of small $\delta\kappa_b$, since δT will then be well approximated by the first-order term in the Taylor expansion of T with respect to $\delta\kappa_b$. To test this property, we compared the sum of the temperature anomalies $(\sum_e \delta T_e)$ to δT_{FB} (see Sections 2.2 and 2.3) along a few representative meridional sections (not shown). The two solutions are very similar at year 1, consistent with the fact that not much signal has yet propagated from each forcing region to other regions. At year 20, the large-scale patterns of $\sum_e \delta T_e$ and δT_{FB} are still similar (by the eye). On the other hand, $\sum_e \delta T_e$ is much noisier with strong mesoscale features superimposed on the large-scale signals. This difference suggests that mesoscale disturbances caused by $\delta\kappa_b$ in one region are not much attenuated in other regions in regional experiments because κ_b is small outside their respective forcing regions, whereas they are attenuated by $\delta\kappa_b$ everywhere in Experiment FB. This difference can be interpreted as a nonlinear effect due to terms like $\delta\kappa_b \delta T_{ezz}$ in Experiment FB.

4.2.2. Vertical structure of κ_b

Although we have restricted forcing by $\delta\kappa_b$ to be depth-independent, a number of studies point toward the importance of its vertical structure. For example, Sasaki et al. (2012) increased the background vertical diffusivity, κ_b, only above the center of the equatorial pycnocline in the equatorial Pacific (analogous to our Regions EQE and EQW), in order to simulate the enhanced mixing recently found there (Richards et al., 2012); they found that the annual-mean sea surface temperature in the eastern equatorial cold tongue is increased, whereas it is decreased in our solutions EQE and EQW (Fig. 8b, upper panels). Fedorov et al. (2010) and Manucharyan et al. (2011) increased $\delta\kappa_b$ only above 200 m to simulate the mixing due to tropical cyclones in tropical and subtropical regions (analogous to our Regions SE, SW, NE, and NW), finding the equatorial cold tongue is significantly warmed, while it changes little in our solutions (upper panels of Figs. 6b, 7b, B.1b, and B.2b). Liu et al. (2012) obtained an optimized, global solution in which the total vertical diffusivity κ was adjusted *at every grid point* in the model, finding that the adjustment to κ from the initial uniform value tends to be large in regions where density changes rapidly (e.g., along fronts and across the pycnocline).

To the extent that linearity to $\delta\kappa_b$ holds, we expect the results in this study to apply even when $\delta\kappa_b$ varies vertically: The generation of anomalies should be governed approximately by 1-d diffusion similar to (7), and dynamical and spiciness components of anomalies should propagate by wave radiation and advection, respectively. On the other hand, since vertical diffusion has the form $(\delta\kappa_b q_z)_z$, the additional term $\delta\kappa_{bz} q_z$ will likely have significant influences in the generation of anomalies, perhaps accounting for the different responses noted in the previous paragraph. In a companion paper (Jia et al., 2014, submitted), we are exploring impacts when $\delta\kappa_b$ varies vertically as well as horizontally.

Acknowledgments

This work is supported by NASA Grant NNX10AE97G. It is also partially supported by JAMSTEC-IPRC Collaborative Study (JICS). We thank Kunihiro Aoki, Shota Katsura, and Young Ho Kim (alphabetical order) for fruitful discussion. Comments from anonymous reviewers helped improve the manuscript. RF, YJ, JPM, NS, and KJR are partially supported by the Japan Agency for Marine-Earth Science and Technology (JAMSTEC), by NASA through Grant NNX07AG53G, and by NOAA through Grant NA11NMF4320128, which sponsor research at the International Pacific Research Center. The authors wish to acknowledge use of the Ferret program for analysis and graphics in this paper. Ferret is a product of NOAA's Pacific Marine Environmental Laboratory. (Information is available at http://ferret.pmel.noaa.gov/Ferret/.)

Appendix A. Difference measures

The dynamical and spiciness components of temperature and salinity anomalies are outlined in Section 2.3 and used in Section 3 to analyze the propagation of anomalies. In this appendix, we first give precise definitions of the two components (A.1), then discuss the methods of their computation (A.2), and then note useful properties of each component (A.3).

A.1. Definitions

One measure of differences between solutions is their difference on z levels,

$$\delta q_e \equiv \hat{q}_e(z, \boldsymbol{r}) - \hat{q}_0(z, \boldsymbol{r}), \tag{A.1a}$$

where q is any model variable, $\hat{q}(z,\boldsymbol{r})$ is the functional form of q in z coordinates, subscript e denotes the test solution from which the variable is taken (FB, EQE, etc.) with $q_0 \equiv q_{\mathrm{CTL}}$ for convenience, and $\boldsymbol{r} \equiv (x,y,t)$. Another is their difference on density levels

$$\delta'' q_e \equiv \tilde{q}_e(\rho,\boldsymbol{r}) - \tilde{q}_0(\rho,\boldsymbol{r}), \tag{A.1b}$$

where $\tilde{q}_e(\rho,\boldsymbol{r})$ is the functional form of q_e in density coordinates. (Throughout this paper, "density" means potential density referenced to the sea surface.) Since the density field is different between solutions, there is no unique way to map $\delta'' q_e$ onto z-coordinates or δq_e onto ρ-coordinates. In this study, we choose the ρ_{CTL} field for the mapping and regard δq_e and $\delta'' q_e$ as regular field variables, independent of coordinate system.

For temperature and salinity it is useful to split δq_e into two parts: $\delta q_e = \delta' q_e + \delta'' q_e$. To make the separation for δT_e (δS_e is treated similarly), note that $\tilde{T}_e(z,\boldsymbol{r}) = \tilde{T}_e[\hat{\rho}_e(z,\boldsymbol{r}),\boldsymbol{r}]$. Then, provided that $\delta\rho_e$ is small, we can write

$$\begin{aligned}\delta T_e &= \hat{T}_e(z,\boldsymbol{r}) - \hat{T}_0(z,\boldsymbol{r}) = \tilde{T}_e[\hat{\rho}_e(z,\boldsymbol{r}),\boldsymbol{r}] - \tilde{T}_0[\hat{\rho}_0(z,\boldsymbol{r}),\boldsymbol{r}]\\ &\simeq \tilde{T}_e[\hat{\rho}_0(z,\boldsymbol{r}),\boldsymbol{r}] + \frac{\partial\tilde{T}_e}{\partial\rho}[\hat{\rho}_0(z,\boldsymbol{r}),\boldsymbol{r}]\delta\rho_e(z,\boldsymbol{r}) - \tilde{T}_0[\hat{\rho}_0(z,\boldsymbol{r}),\boldsymbol{r}]\\ &\equiv \delta' T_e + \delta'' T_e,\end{aligned} \tag{A.2a}$$

where

$$\delta' T_e \equiv \frac{\partial\tilde{T}_e}{\partial\rho}[\hat{\rho}_0(z,\boldsymbol{r}),\boldsymbol{r}]\,\delta\rho_e(z,\boldsymbol{r}) \tag{A.2b}$$

and

$$\delta'' T_e \equiv \tilde{T}_e[\hat{\rho}_0(z,\boldsymbol{r}),\boldsymbol{r}] - \tilde{T}_0[\hat{\rho}_0(z,\boldsymbol{r}),\boldsymbol{r}]. \tag{A.2c}$$

According to (A.2c) the spiciness component $\delta'' T_e$ is the temperature difference taken at constant density between the two solutions: It is just definition (A.1b) expressed in z-coordinates. According to (A.2b), the dynamical component $\delta' T_e$ is proportional to $\delta\rho_e(z,\boldsymbol{r})$, a clear indication that it is associated with the vertical displacement of density surfaces. An alternative (but equivalent) formalism of the separation is presented by Schneider (2004) and the separation is extended to more general cases by Taguchi and Schneider (2014).

A.2. Calculation methods

To compute $\delta'' T_e$, we use its definition (A.1b). To compute $\delta' T_e$, we map $\delta'' T_e$ onto z-coordinates and use $\delta' T_e = \delta T_e - \delta'' T_e$ instead of using (A.2c). To check the accuracy of the approximation (Taylor expansion) in deriving (A.2a), we compare the $\delta' T_e$ computed this way with another computed from (A.2b). For the latter, we first use the approximation

$$(\partial\tilde{T}_e/\partial\rho)\,\delta\rho_e = [\partial(\tilde{T}_0 + \delta'' T_e)/\partial\rho]\,\delta\rho_e \simeq (\partial\tilde{T}_0/\partial\rho)\,\delta\rho_e$$

and then compute $\partial\tilde{T}_0/\partial\rho$ using the z-derivatives of T and ρ via the identity

$$\frac{\partial\tilde{T}}{\partial\rho} = \frac{\partial\hat{T}}{\partial z}\frac{\partial z}{\partial\rho} = \frac{\partial\hat{T}/\partial z}{\partial\rho/\partial z}.$$

We confirmed that the two methods give very similar $\delta' T_e$ fields.

We use annual averages of the temperature and salinity fields to calculate $\delta' T_e$ and $\delta'' T_e$ because using the original (10-day-mean) data would require large computational time and disk space. The resulting anomaly fields are not identical to those in which instantaneous temperature and salinity fields are used to calculate $\delta' T_e$ and $\delta'' T_e$, which are then averaged over one year. To assess the error from the use of annual-mean data, we computed $\delta' T_{\mathrm{FB}}$ using 10-day-mean data of Solutions CTL and FB for year 20. We found that $\delta' T_{\mathrm{FB}}$ is virtually indistinguishable using the two methods except in and just below the mixed layer, a consequence of seasonality in $\delta' T_e$ being very small below the mixed layer.

A.3. Properties

Expression (A.2c) indicates that $\delta' T_e$ is in one-to-one correspondence with $\delta\rho_e$ with the given background field $\partial\tilde{T}_e/\partial\rho \approx \partial\tilde{T}_0/\partial\rho$ acting as a factor to modulate its amplitude. As a result, $\delta' T_e$ is clearly dynamically active, being associated with a pressure anomaly and wave propagation. Note that its salinity counterpart, $\delta' S_e$, is less useful in the tropical Pacific as an indicator of active dynamics because $\partial\tilde{S}_0/\partial\rho$ takes both signs and can even vanish[2] so that $\delta' S_e$ does not have a consistent correspondence with a pressure anomaly.

The spiciness anomaly, $\delta'' T_e$, behaves like a passive tracer. Below the mixed layer, the difference of temperature equations written in density coordinates between a test run e and the control run is

$$\begin{aligned}&\partial_t\delta'' T_e + \boldsymbol{u}_0\cdot\nabla\delta'' T_e + \delta''\boldsymbol{u}\cdot\nabla T_0 + \delta''(\text{diapycnal advection})\\ &\quad\approx \delta''(\kappa_{\mathrm{b}}\partial_{zz}T) + \delta''(\text{horizontal diffusion}),\end{aligned} \tag{A.3}$$

where $\boldsymbol{u}_0$ and $\delta''\boldsymbol{u}$ are horizontal velocity vectors for the control run and the difference solution, ∇ is the horizontal gradient operator, and the r.h.s. is assumed to be transformed into density coordinates after being evaluated in z-coordinates. The first term on the r.h.s. includes the generation of spiciness anomalies in the forcing region where $\delta\kappa_{\mathrm{b}} \neq 0$ (Section 3.2.2). The first and second terms on the l.h.s. represent pure advection, $\partial_t + \boldsymbol{u}_0\cdot\nabla$, of the spiciness anomaly by the background flow. The third term represents the advection of the background temperature field by the anomalous flow, $\delta''\boldsymbol{u}$. Diapycnal advection is small below the mixed layer and outside the forcing region. Likewise, horizontal diffusion is small, if anything tending to smooth the $\delta'' T_e$ field.

Most of the discussion of $\delta'' T_e$ in the main text concerns its local generation and advection by the background flow $\boldsymbol{u}_0$. Near the equator, there are a few instances where advection by $\delta''\boldsymbol{u}$ is also significant. In these cases, it is useful to interpret $\delta''\boldsymbol{u}\cdot\nabla T_0$ as an additional forcing term in which $\delta''\boldsymbol{u}$ is generated by dynamical processes, predominantly by wave propagation associated with $\delta' T_e$ (see Appendices B.3 and B.4).

Finally, it is noteworthy that $\delta'' T_e$ is associated with a salinity anomaly of the same sign. That is, $0 = \delta''\rho_e = \bar{\rho}(-\alpha\delta'' T_e + \beta\delta'' S_e)$ so that $\delta'' S_e = (\alpha/\beta)\delta'' T_e$. If typical values of α and β are used, a 1°C temperature anomaly is associated with about a 0.3 psu salinity anomaly.

Appendix B. Other regional solutions

In Section 3.3, we reported regional solutions that most clearly illustrate basic processes. Here, we discuss the other regional solutions, focusing on their differences from those in the main text. They mostly support and clarify the processes discussed in the main text, with a few new processes introduced here as well.

B.1. Solution SW

The vertical structures of Solutions SW and SE are very similar in the latitude band of the forcing, a consequence of T_{0zz} and S_{0zz} being much the same in each region (compare left panels of Figs. B.1a and 6a along 170°E and 130°W, respectively). One difference is that, because isolines of T_0 and S_0 are deeper in the western Pacific, anomalies in Solution SW occur somewhat deeper in the water column. Other notable differences are that the deep, positive area of $\delta' T_{\mathrm{SW}}$ is much weaker than in Solution SE owing to T_{0zz}

[2] This expression is the partial derivative of $\tilde{S}(\rho,x,y,t)$ at fixed x,y, and t and not to be confused with the similar-looking relation from the equation of state of sea water: $\partial S/\partial\rho$ at fixed T and p.

Please cite this article in press as: Furue, R., et al. Impacts of regional mixing on the temperature structure of the equatorial Pacific Ocean. Part 1: Vertically uniform vertical diffusion. Ocean Modell. (2015), http://dx.doi.org/10.1016/j.ocemod.2014.10.002

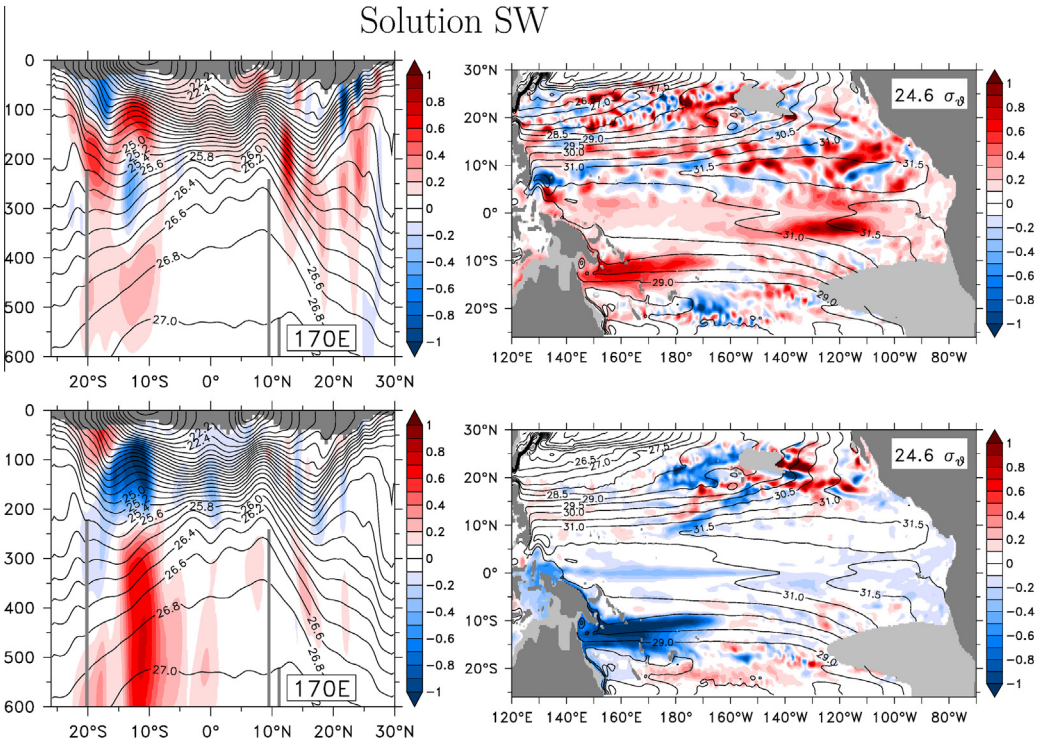

Fig. B.1a. Same as Fig. 6a but for Solution SW and for 170°E (left) and the 24.6-σ_θ surface (upper-right).

being smaller, and that the shallow positive patch of $\delta' T_{SW}$ is more prominent.

The horizontal structures of the dynamical and spiciness signals differ from Solution SE most prominently in that their locally forced responses are confined to the western-Pacific forcing region (right panels of Figs. B.1a and 6a). The dynamical signals on both the 24.6-σ_θ and 26.6-σ_θ surfaces extend to the equator along the western boundary and then spread throughout the basin, just as the 26.6-σ_θ signal does in Solution SE (top-right panels of Figs. B.1a and 6a). A notable difference is that the dynamical signal on 24.6-σ_θ equatorward of the latitude band of the forcing is somewhat stronger (Figs. B.1a, upper-right) than in Solution SE (not shown). On this isopycnal, there is a distinct band of strong positive $\delta' T_{SW}$ centered at 120°W and 3°S. This feature likely results from interaction between the Rossby-wave packet and the shallow tight pycnocline there; a similar feature is visible in the 130°W section of $\delta' T_{SE}$ (Fig. 6a, upper-left) and in many of the other solutions below. The spiciness response differs from that in Solution SW in that it does not extend to the equator in the interior ocean, since Region SW lies west of the interior pathway of the South Pacific STC (bottom-right panels of Fig. B.1a and 6a). The absence of the interior pathway allows the equatorial tongue of negative $\delta'' T_{SW}$ that emanates from the western boundary to be much more apparent.

Along the equator (Fig. B.1b), there is a shallow band of positive $\delta' T_{SW}$ within the pycnocline, the equatorial extension of the anomaly from Region SW (Fig. B.1a, upper-right). Because of this positive band, the negative δT_{SW} anomaly within the pycnocline is much weaker than in Solution SE, as the bands of negative $\delta'' T_{SW}$ and positive $\delta' T_{SW}$ anomalies tend to cancel. Below the pycnocline, the deep positive $\delta'' T_{SW}$ anomaly is stronger because it is closer to its forcing region.

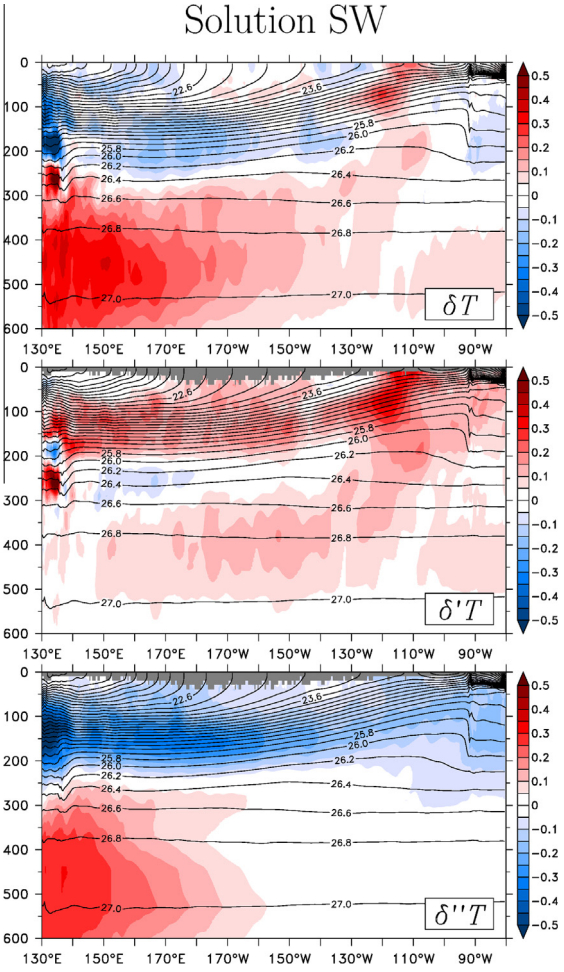

Fig. B.1b. Same as Fig. 6b but for Solution SW.

B.2. Solution NW

Owing to the large zonal gradients of the mean T and S fields, the vertical structures of the local anomalies for Solution NW are

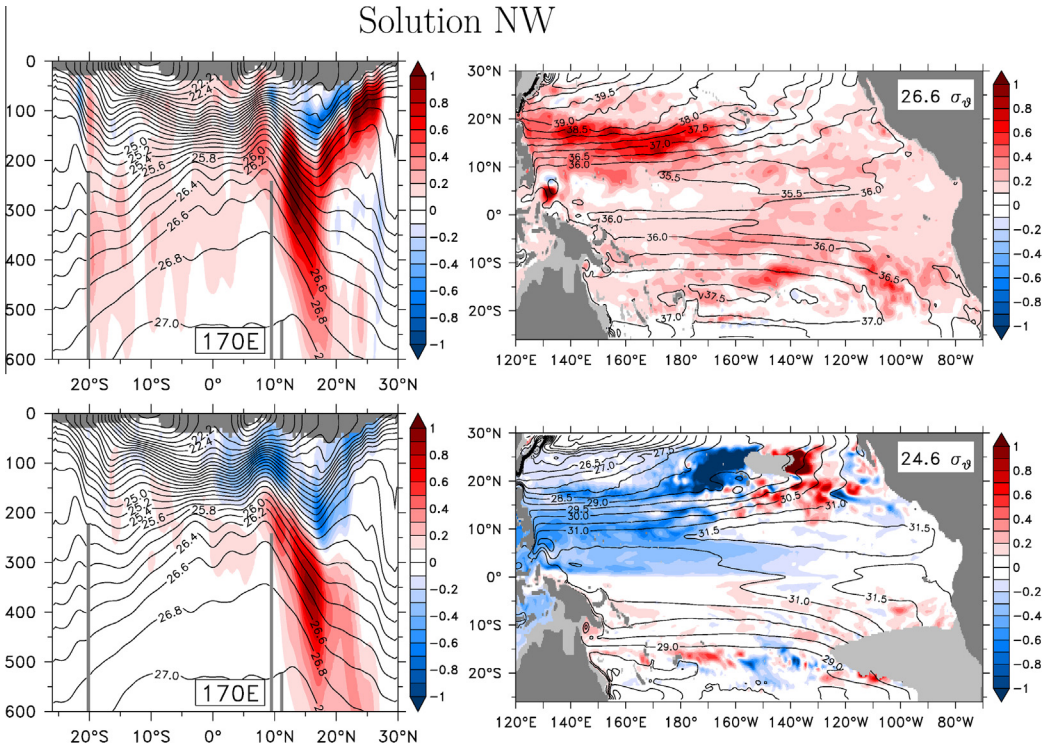

Fig. B.2a. Same as Fig. 6a but for Solution NW and for 170°E (left).

quite different from those for Solution NE, with both $\delta' T_{\mathrm{NW}}$ and $\delta'' T_{\mathrm{NW}}$ lacking negative anomalies at depth (compare left panels of Figs. B.2a and 7a). Nevertheless, the horizontal structures of the signals are similar, as they are spread about the basin by the same processes (right panels of Fig. B.2a and 7a). Note that, because the locally forced response is confined to the western ocean, advection of $\delta'' T_{\mathrm{NW}}$ by the NECC is much more apparent. Consistent with the vertical structure of the local anomalies, along the equator $\delta' T_{\mathrm{NW}}$ has only a single, deep band and $\delta'' T_{\mathrm{NW}}$ has both negative and positive bands in the middle and lower pycnocline, respectively (compare Figs. B.2b and 7b).

Interestingly, the red and blue patches east and west of the outcropping are still present in Solution NW (compare bottom-right panels of Figs. B.2a and 7a), although the red one is considerably weaker than in Solution NE. The 1-d mixing model predicts weak $\delta'' T$ of both signs west of the outcrop on 24.6 σ_θ (not shown) but a coherent negative anomaly emerges after several years of integration and dominates this region from the mixed layer down to the $\sim$ 25.4-σ_θ isopycnal (not shown). The positive anomaly east of the outcrop occurs east of Region NW and also emerges only after several years. Neither of these anomalies, then, can be explained by 1-d mixing, and their cause is likely gradual changes in mixed-layer properties as the solution adjusts toward equilibrium, similar in nature to the mixed-layer changes discussed at the end of Section 3.3.1.

B.3. Solutions ESE and ESW

The vertical structure of the locally-generated dynamical field of Solution ESE differs considerably from that of Solution SE (compare Figs. B.3a and 6a, top-left panels), with $\delta' T_{\mathrm{ESE}}$ having only a single, prominent, positive anomaly within the lower pycnocline. As for the other solutions, the local dynamical response spreads throughout the basin via wave radiation, forming a basin-wide recirculation confined to the latitude band of the forcing, with a weaker, wedge-shaped, Rossby-wave packet extending from the eastern boundary (Fig. B.3a; top-right panel). In addition, because

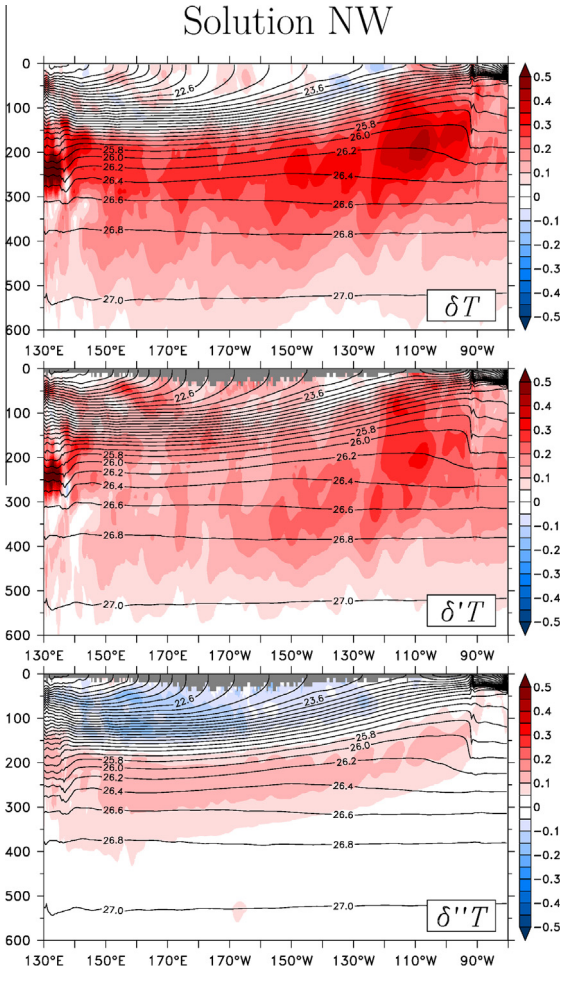

Fig. B.2b. Same as Fig. 6b but for Solution NW.

Please cite this article in press as: Furue, R., et al. Impacts of regional mixing on the temperature structure of the equatorial Pacific Ocean. Part 1: Vertically uniform vertical diffusion. Ocean Modell. (2015), http://dx.doi.org/10.1016/j.ocemod.2014.10.002

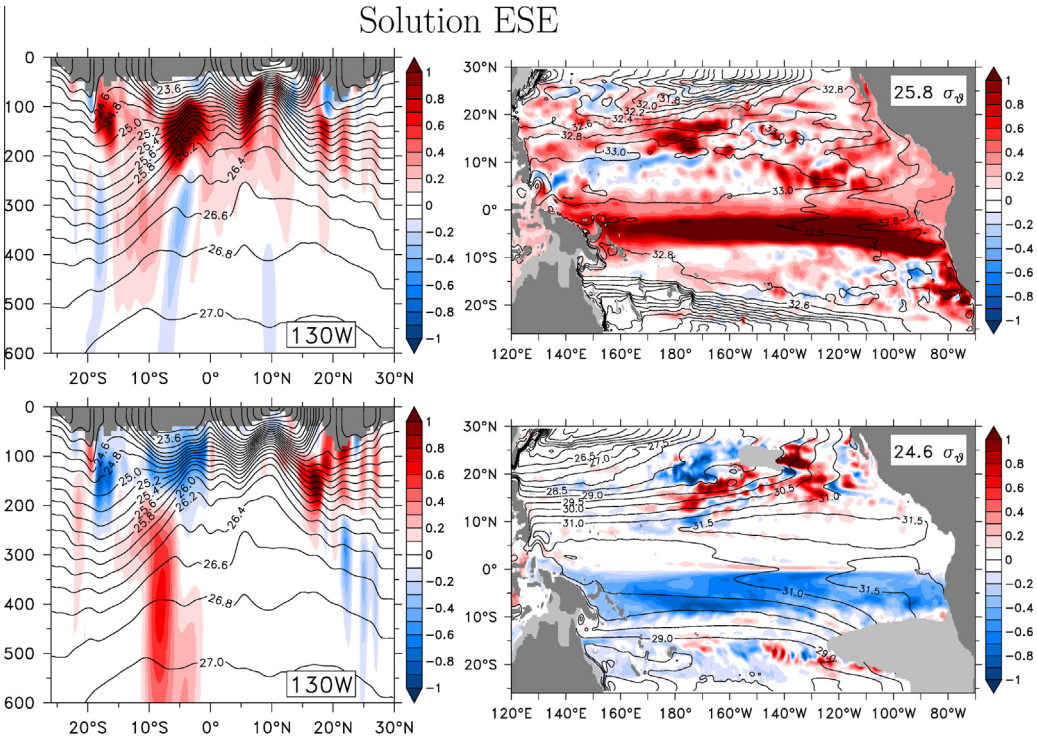

Fig. B.3a. Same as Fig. 6a but for Solution ESE and for the 25.8-σ_θ surface (upper-right).

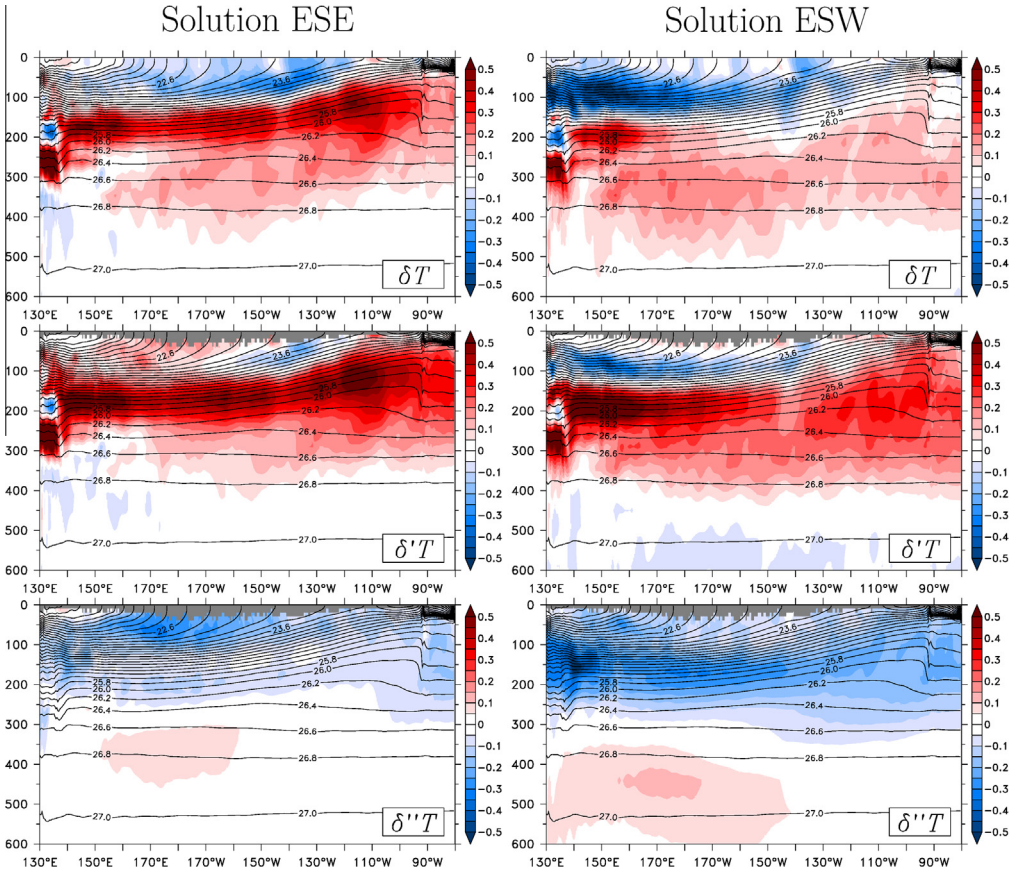

Fig. B.3b. Same as Fig. 6b but for Solutions ESE (left) and ESW (right).

Please cite this article in press as: Furue, R., et al. Impacts of regional mixing on the temperature structure of the equatorial Pacific Ocean. Part 1: Vertically uniform vertical diffusion. Ocean Modell. (2015), http://dx.doi.org/10.1016/j.ocemod.2014.10.002

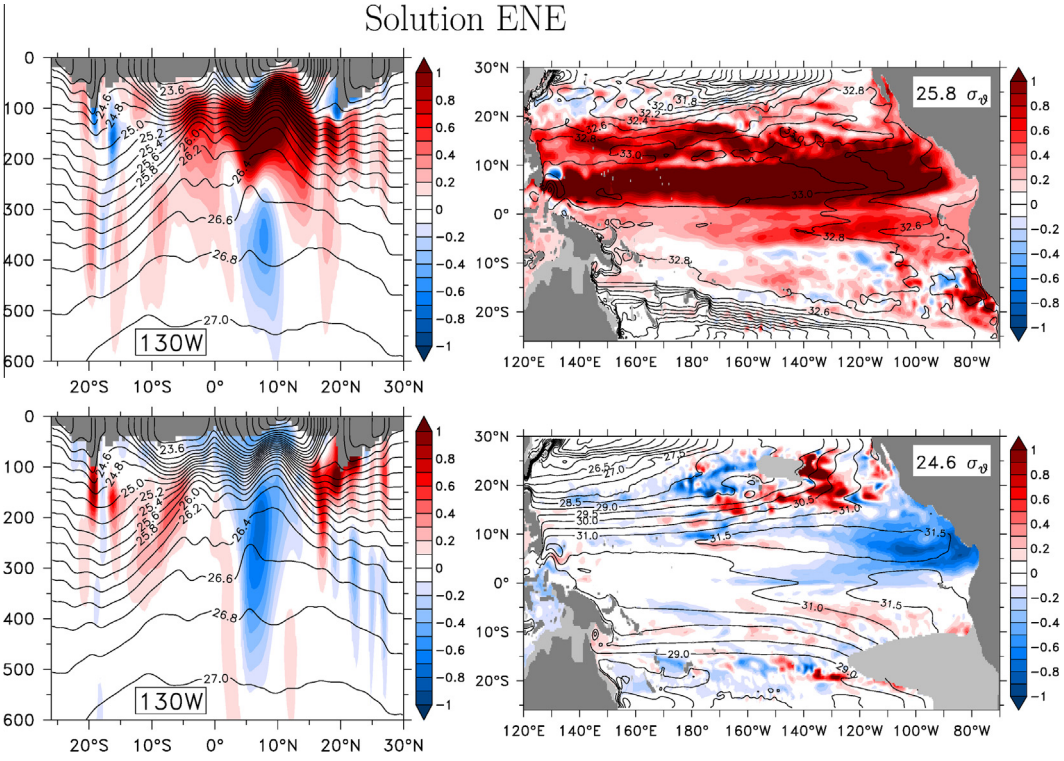

Fig. B.4a. Same as Fig. 6a but for Solution ENE and for the 25.8-σ_θ surface (upper-right).

the forcing region lies so close to the equator, it directly forces equatorial waves, which extend north of the equator (see below).

In contrast to $\delta' T_{\mathrm{ESE}}$, the vertical structure of $\delta'' T_{\mathrm{ESE}}$ is very similar to that of Solution SE (compare bottom-left panels Figs. B.3a and 6a in the latitude bands of their respective forcings). The locally-generated, negative, spiciness signal is advected westward by the South Equatorial Current (SEC) and equatorward within the subsurface branch of the South Pacific STC (Fig. B.3a, bottom-right panel). Because Region ESE is located close to the equator, however, most of it advects to the equator via the interior STC pathway, with little following the western-boundary pathway into the Indonesian Seas. As a result, there is much less negative spiciness anomaly on the northern side of the equator than in Solution SE (lower-right panels of Figs. B.3a and 6a). Interestingly, there is a narrow patch of *positive* spiciness anomaly just north of the equator. Since Region ESE does not extend to the equator this patch cannot be due to local mixing. The cause of the positive anomaly is likely a response to advection of the background T and S fields by the velocity anomaly, $\delta \boldsymbol{u}$, due to this directly-forced response mentioned above.[3]

Along the equator, δT_{ESE} is very different from δT_{SE} (compare Figs. B.3b and 6b), a consequence of the propagation of the strong, locally-generated, positive $\delta' T_{\mathrm{ESE}}$ anomaly in the lower pycnocline to the equator. There is also a patch of negative $\delta' T_{\mathrm{ESE}}$ in the upper pycnocline east of ~160°W, which is due to the direct forcing of equatorial waves. In contrast, $\delta'' T_{\mathrm{ESE}}$ is similar to $\delta'' T_{\mathrm{SE}}$, both having a negative signal within and above the pycnocline. In Solution ESE, however, the signal is significantly weaker because of the across-equatorial reversal of $\delta'' T_{\mathrm{ESE}}$ (Fig. B.3a, bottom panels): The instantaneous spiciness field at the equator shows mesoscale patches of alternating signs associated with Tropical Instability Waves (not shown); as a result, the annual mean of $\delta'' T_{\mathrm{ESE}}$ is close to zero near the mid-pycnocline, where the negative and positive anomalies average out. In the western ocean, the deep, positive $\delta'' T_{\mathrm{ESE}}$ anomaly (300–400 m, 150°E–160°W) is the westward extension of the locally-generated deep anomaly (Fig. B.3a); it appears only in the west because the southern Tsuchiya Jet shifts equatorward toward the west due to the equatorward bending of Rossby-wave characteristics (McCreary et al., 2002; Furue et al., 2007, 2009).

The dynamical and spiciness responses in Solution ESW are very similar to their counterparts in Solution ESE in Fig. B.3a, the primary differences being that they are shifted somewhat deeper and the local responses are confined west of 170°W. The negative $\delta' T_{\mathrm{ESW}}$ signal in the upper pycnocline is more prominent than in Solution ESE (not shown), presumably because the upper pycnocline is better separated from the mixed layer in the west, and this anomaly propagates eastward as a Kelvin wave. As in Solution ESE, there is a positive anomaly of $\delta'' T_{\mathrm{ESW}}$ just north of the equator in the pycnocline, but it is broader, weaker, and located somewhat farther to the north than in Solution ESE. Along the equator, anomalies are also similar (compare left and right panels of Fig. B.3b), except that $\delta' T_{\mathrm{ESW}}$ is weaker and more vertically diffuse in the eastern ocean (since it is not locally forced there), and the directly generated negative $\delta' T_{\mathrm{ESW}}$ signal in the upper pycnocline is more prominent and $\delta'' T_{\mathrm{ESW}}$ is stronger in the lower pycnocline (because it is not canceled by the positive anomaly north of the equator, which is located mostly outside the averaging window of 1°S–1°N). As a result, the negative spiciness partially cancels the positive dynamical signal.

B.4. Solutions ENE and ENW

The structures of the anomaly fields of Solution ENE are very similar to those of Solution NE (compare Figs. B.4a and 7a). The primary difference is that $\delta'' T_{\mathrm{ENE}}$ on the 24.6-σ_θ density surface (bottom-right panels) does not spread directly across the ocean

[3] Pure advection cannot produce an anomaly of opposite sign and therefore it must be due to the term $\delta \boldsymbol{u} \cdot \nabla T_0$ in (A.3) under the assumption that diffusion is negligible outside the forcing region.

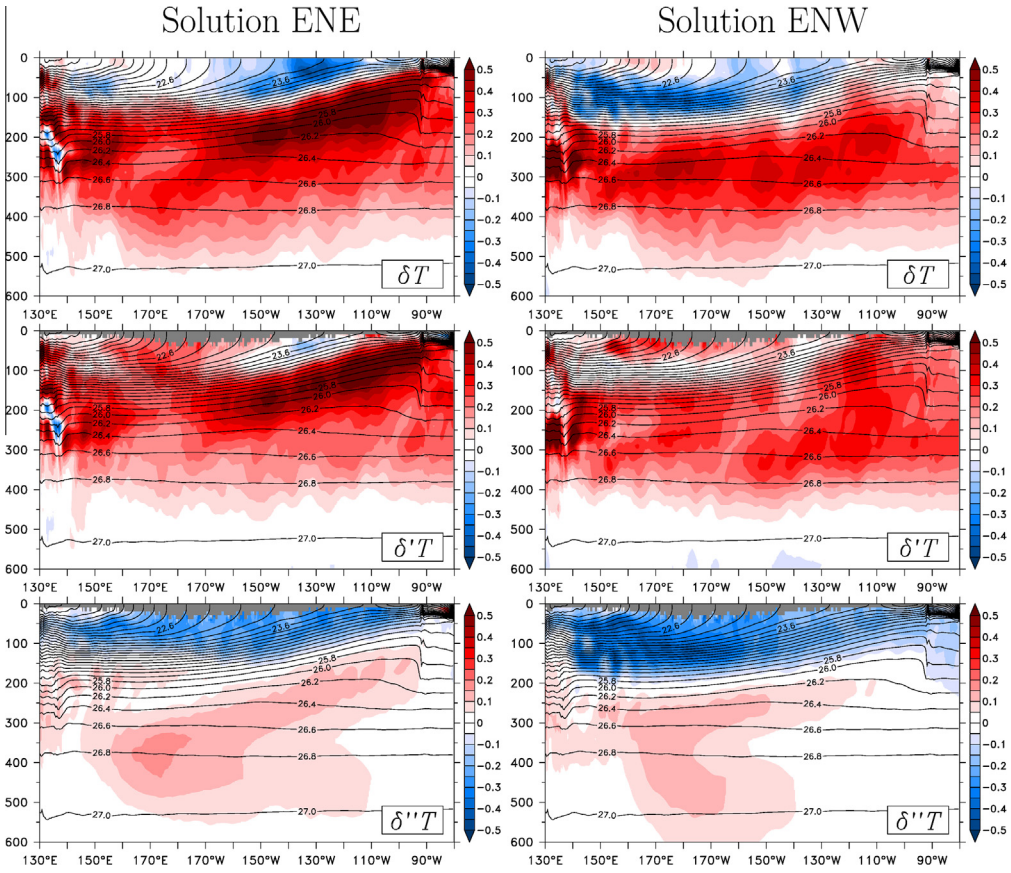

Fig. B.4b. Same as Fig. 6b but for Solutions ENE (left) and ENW (right).

because of the presence of the NECC; instead, it first advects equatorward in the far-eastern ocean where the NECC is weak, and then advects westward and equatorward before joining the northern flank of the EUC east of ∼140°W. Another difference is the band of negative $\delta'' T_{\mathrm{ENE}}$ that exists on both sides of the EUC east of ∼170°W. This anomaly emerges as early as year 1 before the δ''T signal reaches the equator from the forcing region. The cause of the negative anomaly is likely a response to advection of the background T and S fields by the velocity anomaly, $\delta \boldsymbol{u}$, due to the directly-forced equatorial response, a counterpart of the positive $\delta'' T$ in Solution ESE (Appendix B.3). The sign of this $\delta'' T_{\mathrm{ENE}}$ is negative because the sign of $\delta \boldsymbol{u}$ is opposite (not shown). An apparent difference from Solution NE is the lack of a blue band in $\delta' T_{\mathrm{ENE}}$ (top-right panels), but it is absent only because the map is plotted on the shallower 25.8-σ_θ surface.

The equatorial response (Fig. B.4b) is very similar to that of Solution ESE, differences in $\delta' T$ resulting from modest differences in the depth range of the locally generated anomalies. The negative spiciness signal is somewhat stronger in the eastern upper pycnocline than in Solution ESE (Fig. B.3b) because the equatorial anomaly due to $\delta \boldsymbol{u}$ is also negative and is not canceled by a positive signal as it is in Solution ESE (Appendix B.3). The positive spiciness anomaly below the pycnocline is not generated by advection of $\delta'' T_{\mathrm{ENE}}$ by the background circulation. Rather, it results from the advection of the background T and S fields by an anomalous velocity field, $\delta \boldsymbol{u}$, that is part of the dynamical response (Appendix A.3); The signal so generated is then advected eastward in the lower part of the EUC and in the deep, eastward current below the Equatorial Intermediate Current (top-right panel of Fig. 2).

The vertical distributions of $\delta' T_{\mathrm{ENW}}$ and $\delta'' T_{\mathrm{ENW}}$ are similar to those for Solution ENE (left and right panels of Fig. B.4a), except that they lie somewhat deeper because of the deeper overall stratification and that the deep, negative spiciness anomaly is almost gone. Their horizontal patterns (not shown) are roughly mirror images of those in Solution ESW (not shown), except that the locally forced $\delta'' T_{\mathrm{ENW}}$ spreads much more efficiently eastward due to the NECC. As in Solutions NE and NW, the negative $\delta'' T_{\mathrm{ENW}}$ signal in the pycnocline advects in the western boundary current and into the EUC to form a tongue of negative $\delta'' T$; unlike in Solution ENE, the spiciness response to $\delta \boldsymbol{u}$ along the equator seems to be negligible, consistent with the fact that the positive $\delta'' T$ signal along the equator is much weaker in Solution ESW than in ESE (Appendix B.3). The anomalies are also similar to those of Solution ENE along the equator, differing primarily in that the fields are somewhat stronger in the west and weaker in the east due to the shift in position of the forcing (compare right and left panels of Fig. B.4b).

References

Anderson, D.L.T., 1976. The low-level jet as a western boundary current. Mon. Weather Rev. 104 (907–921), 1040.

Fedorov, A.V., Brierley, C.M., Emanuel, K., 2010. Tropical cyclones and permanent El Niño in the early Pliocene epoch. Nature 463, 1066–1071. http://dx.doi.org/10.1038/nature08831.

Ffield, A., Gordon, A.L., 1992. Vertical Mixing in the Indonesian Thermocline. J. Phys. Oceanogr. 22, 184–195.

Ffield, A., Gordon, A.L., 1996. Tidal mixing signatures in the Indonesian Seas. J. Phys. Oceanogr. 26, 1924–1937.

Friedrich, T., Timmermann, A., Decloedt, T., Luther, D.S., Mouchet, A., 2011. The effect of topography-enhanced diapycnal mixing on ocean and atmospheric circulation and marine biogeochemistry. Ocean Modell. 39, 262–274. http://dx.doi.org/10.1016/j.ocemod.2011.04.012.

Furue, R., McCreary, J.P., Yu, Z., 2009. Dynamics of the northern Tsuchiya Jet. J. Phys. Oceanogr. 39, 2024–2051.

Furue, R., McCreary, J.P., Yu, Z., Wang, D., 2007. Dynamics of the southern Tsuchiya Jet. J. Phys. Oceanogr. 37, 531–553.

Furue, R., Nakajima, K., Ishikawa, I., 1995. Modal decomposition of deep ocean circulation models: comparison with reduced-gravity models. J. Geophys. Res. 100, 10567–10588.
Godfrey, J.S., Hirst, A.C., Wilkin, J., 1993. Why does the Indonesian throughflow appear to originate from the North Pacific? J. Phys. Oceanogr. 23, 1087–1098.
Hasumi, H., Suginohara, N., 1999. Effects of locally enhanced vertical diffusivity over rough bathymetry on the world ocean circulation. J. Geophys. Res. 104, 23367–23374.
Hoteit, I., Cornuelle, B., Heimbach, P., 2010. An eddy-permitting, dynamically consistent adjoint-based assimilation system for the tropical pacific: hindcast experiments in 2000. J. Geophys. Res. 115. http://dx.doi.org/10.1029/2009JC005437.
Hoteit, I., Cornuelle, B., Thierry, V., Stammer, D., 2008. Impact of resolution and optimized ECCO forcing on simulations of the Tropical Pacific. J. Oceanic Atmos. Tech. 25, 131–147.
Jayne, S.R., St. Laurent, L.C., 2001. Parameterizing tidal dissipation over rough topography. Geophys. Res. Lett. 28, 811–814. http://dx.doi.org/10.1029/2000GL012044.
Jia, Y., Furue, R., McCreary, J.P., 2014. Impacts of regional mixing on the temperature structure of the equatorial Pacific Ocean. Part 2: Depth-dependent vertical diffusion, submitted for publication.
Jochum, M., 2009. Impact of latitudinal variations in vertical diffusivity on climate simulations. J. Geophys. Res. 114. http://dx.doi.org/10.1029/2008JC005030.
Johnson, G.C., Sloyan, B.M., Kessler, W.S., McTaggart, K.E., 2002. Direct measurements of upper ocean currents and water properties across the tropical Pacific during the 1990s. Prog. Oceanogr. 52, 31–61.
Kashino, Y., Aoyama, M., Kawano, T., Hendiarti, N., Syaefudin, Anantasena, Y., Muneyama, K., Watanabe, H., 1996. The water masses between mindanao and new guinea. J. Geophys. Res. 101, 12391–12400. http://dx.doi.org/10.1029/95JC03797.
Kawase, M., 1987. Establishing of deep ocean circulation driven by deep-water production. J. Phys. Oceanogr. 17, 2294–2317.
Kim, Y.H., Kug, J.-S., Yim, B.Y., Furue, R., 2014. Response of the ENSO to Tidal Mixing in equatorial Pacific, in preparation.
Köhl, A., Stammer, D., 2008. Variability of the meridional overturning in the North Atlantic from the 50-year GECCO state estimation. J. Phys. Oceanogr. 38, 1913–1930.
Köhl, A., Stammer, D., Cornuelle, B., 2007. Interannual to decadal changes in the ECCO global synthesis. J. Phys. Oceanogr. 37, 313–337.
Large, W.G., McWilliams, J., Doney, S., 1994. Oceanic vertical mixing: a review and a model with a nonlocal boundary layer parameterization. Rev. Geophys. 32, 363–403.
Large, W.G., Pond, S., 1981. Open ocean momentum flux measurements in moderate to strong winds. J. Phys. Oceanogr. 11, 324–336.
Large, W.G., Pond, S., 1982. Sensible and latent heat flux measurements over the ocean. J. Phys. Oceanogr. 12, 464–482.
Liu, C., Köhl, A., Stammer, D., 2012. Adjoint-based estimation of eddy-induced tracer mixing parameters in the global ocean. J. Phys. Oceanogr. 42, 1186–1206.
Lu, P., McCreary, J.P., 1995. Influence of the ITCZ on the flow of thermocline water from the subtropical to the equatorial Pacific Ocean. J. Phys. Oceanogr. 25, 3076–3088.
Lukas, R., 1986. The termination of the equatorial undercurrent in the eastern Pacific. Prog. Oceanogr. 16, 63–90.
Luyten, J., Stommel, H., 1986. Gyres driven by combined wind and buoyancy flux. J. Phys. Oceanogr. 16, 1551–1560.
Manucharyan, G.E., Brierley, C.M., Fedorov, A.V., 2011. Climate impacts of intermittent upper ocean mixing induced by tropical cyclones. J. Geophys. Res. 116. http://dx.doi.org/10.1029/2011JC007295.
Marshall, J., Adcroft, A., Hill, C., Perelman, L., Heisey, C., 1997. A finite-volume, incompressible Navier–Stokes model for studies of the ocean on parallel computers. J. Geophys. Res. 102, 5753–5766.
Maximenko, N.A., Melnichenko, O.V., Niller, P.P., Sasaki, H., 2008. Stationary mesoscale jet-like features in the ocean. Geophys. Res. Lett. 35. http://dx.doi.org/10.1029/2008GL033267.
McCreary, J.P., 1981. A linear stratified ocean model of the equatorial undercurrent. Phil. Trans. R. Soc. A 298, 603–635.
McCreary, J.P., Lu, P., 1994. Interaction between the subtropical and equatorial ocean circulations: the subtropical cell. J. Phys. Oceanogr. 24, 466–497.
McCreary, J.P., Lu, P., Yu, Z., 2002. Dynamics of the Pacific subsurface countercurrents. J. Phys. Oceanogr. 32, 2379–2404.
McCreary, J.P., Miyama, T., Furue, R., Jensen, T., Kang, H.W., Bang, B., Qu, T., 2007. Interactions between the Indonesian throughflow and circulations in the Indian and Pacific Oceans. Prog. Oceanogr. 75, 70–114.
Meehl, G.A., Gent, P.R., Arblaster, J.M., Otto-Bliesner, B.L., Brady, E.C., Craig, A., 2001. Factors that affect the amplitude of El Nino in global coupled climate models. Clim. Dyn. 17, 515–526.
Montes, I., Colas, F., Capet, X., Schneider, W., 2010. On the pathways of the equatorial subsurface currents in the eastern equatorial Pacific and their contributions to the Peru–Chile undercurrent. J. Geophys. Res. 115. http://dx.doi.org/10.1029/2009JC005710.
Nakano, H., Hasumi, H., 2005. A series of zonal jets embedded in the broad zonal flows in the Pacific obtained in eddy-permitting ocean general circulation models. J. Phys. Oceanogr. 35, 474–488.
Nonaka, M., Xie, S.P., 2000. Propagation of North Pacific interdecadal subsurface temperature anomalies in an ocean GCM. Geophys. Res. Lett. 27, 3747–3750.
Penven, P., Echevin, V., Pasapera, J., Colas, F., Tam, J., 2005. Average circulation, seasonal cycle, and mesoscale dynamics of the Peru current system: a modeling approach. J. Geophys. Res. 110. http://dx.doi.org/10.1029/2005JC002945.
Richards, K.J., Kashino, Y., Natarov, A., Firing, E., 2012. Mixing in the western equatorial Pacific and its modulation by ENSO. Geophys. Res. Lett. 39. http://dx.doi.org/10.1029/2011GL050439.
Richards, K.J., Maximenko, N.A., Bryan, F.O., Sasaki, H., 2006. Zonal jets in the Pacific Ocean. Geophys. Res. Lett. 33. http://dx.doi.org/10.1029/2005GL024645.
Richards, K.J., Xie, S.P., Miyama, T., 2009. Vertical mixing in the ocean and its impact on the coupled ocean–atmosphere system in the eastern tropical Pacific. J. Clim. 22, 3703–3719. http://dx.doi.org/10.1175/2009JCLI2702.1.
Roemmich, D., Gilson, J., 2009. The 2004–2008 mean and annual cycle of temperature, salinity, and steric height in the global ocean from the Argo program. Prog. Oceanogr. 82, 81–100.
Sasaki, W., Richards, K.J., Luo, J.J., 2012. Role of vertical mixing originating from small vertical scale structures above and within the equatorial thermocline in an OGCM. Ocean Modell. 57–58, 29–42.
Sasaki, W., Richards, K.J., Luo, J.J., 2013. Impact of vertical mixing induced by small vertical scale structures above and within the equatorial thermocline on the tropical pacific in a CGCM. Clim. Dyn. 41, 443–453.
Schneider, N., 2004. The response of tropical climate to the equatorial emergence of spiciness anomalies. J. Clim. 17, 1083–1095.
Spall, M.A., 2000. Buoyancy-forced circulations around islands and ridges. J. Mar. Res. 58, 957–982.
Suga, t., Kato, A., Hanawa, K., 2000. North Pacific tropical water: its climatology and temporal changes associated with the climate regime shift in the 1970s. Prog. Oceanogr. 47, 223–256.
Taguchi, B., Schneider, N., 2014. Origin of decadal-scale, eastward-propagating heat content anomalies in the North Pacific. J. Clim. 27, 7568–7586. http://dx.doi.org/10.1175/JCLI-D-13-00102.1.
Talley, L.D., 1985. Ventilation of the subtropical North Pacific: the shallow salinity minimum. J. Phys. Oceanogr. 15, 633–649, http://dx.doi.org/10.1175/1520-0485(1985)015<0633:VOTSNP>2.0.CO;2.
Tatebe, H., Hasumi, H., 2010. Formation mechanism of the Pacific equatorial thermocline revealed by a general circulation model with a high accuracy tracer advection scheme. Ocean Modell. 35, 245–252.
Tsuchiya, M., 1968. Upper Waters of the Intertropical Pacific Oceans. Johns Hopkins Oceanographic Studies, vol. 4. Johns Hopkins Press.
Tsuchiya, M., 1972. A subsurface north equatorial countercurrent in the eastern Pacific Ocean. J. Geophys. Res. 77, 5981–5986.
Tsuchiya, M., 1975. Subsurface countercurrents in the eastern equatorial Pacific Ocean. J. Mar. Res. 33 (Suppl.), 145–175.
Tsuchiya, M., 1981. The origin of the Pacific equatorial 13 °C water. J. Phys. Oceanogr. 11, 794–812.
Wyrtki, K., 1962. The subsurface water masses in the western South Pacific Ocean. Mar. Freshwater Res. 13, 18–47. http://dx.doi.org/10.1071/MF9620018.

Please cite this article in press as: Furue, R., et al. Impacts of regional mixing on the temperature structure of the equatorial Pacific Ocean. Part 1: Vertically uniform vertical diffusion. Ocean Modell. (2015), http://dx.doi.org/10.1016/j.ocemod.2014.10.002